

5-2019

Gallium Nitride Microcantilever Heater Based VOC Sensors and Monitoring System Development

Sean Sterling Gorman
Clemson University, ssgorman11@gmail.com

Follow this and additional works at: https://tigerprints.clemson.edu/all_theses

Recommended Citation

Gorman, Sean Sterling, "Gallium Nitride Microcantilever Heater Based VOC Sensors and Monitoring System Development" (2019).
All Theses. 3130.
https://tigerprints.clemson.edu/all_theses/3130

This Thesis is brought to you for free and open access by the Theses at TigerPrints. It has been accepted for inclusion in All Theses by an authorized administrator of TigerPrints. For more information, please contact kokeefe@clemson.edu.

GALLIUM NITRIDE MICROCANTILEVER HEATER BASED VOC SENSORS AND
MONITORING SYSTEM DEVELOPMENT

A Thesis
Presented to
the Graduate School of
Clemson University

In Partial Fulfillment
of the Requirements for the Degree
Master of Science
Electrical Engineering

by
Sean Sterling Gorman
May 2019

Accepted by:
Goutam Koley, Committee Chair
William Harrell
Apparao Rao

ABSTRACT

The modern health risk associated with Volatile Organic Compounds (VOCs) requires a response on multiple fronts including industrial, workplace, and residential changes. To begin enacting change the sensitive, selective, portable, and inexpensive detection of VOCs to identify and eliminate their sources needs to be addressed. No current technology adequately meets these requirements, however AlGaN/GaN microcantilever heaters have shown good potential to do so.

In this work single channel microcantilever heaters were designed, characterized, and tested with VOCs, and the VOCs were identifiable based on the slope of the sensor current. The single channel devices were employed in a portable functioning VOC sensing system, and further work was done to create a WIFI enabled system that could bring the sensors onto the Internet of Things.

The impact of VOC exposure on the electrical breakdown of GaN in the inter channel region of dual channel microcantilever heaters has been studied. Exposure to three different VOCs with different latent heats of evaporation resulted in changes in breakdown voltage of varying magnitude that can be correlated to their latent heats of evaporation. A physical model has been proposed to explain the observed shift in breakdown voltage upon VOC exposure based on changes in thermal and electrical profiles at the microcantilever apex, which is caused by the molecular interaction and amplified by its unique tapered geometry. The critical breakdown field of the inter channel GaN has been observed to reduce dramatically by almost 50 times compared to that of bulk GaN at room temperature. The inter-channel or breakdown current rises

dramatically at the onset of breakdown induced by VOC exposure, at specific bias voltages corresponding to VOCs, which can be utilized for detecting them with high sensitivity as well as selectivity.

Also discussed is a study to monitor indoor air quality by measuring multiple environmental parameters of residential spaces that are home to children with documented respiratory ailments (such as asthma) and attempt to correlate sensing results and medical incidents on a weekly basis.

DEDICATION

This work is dedicated to my family and friends who supported me along the way.

ACKNOWLEDGMENTS

I would like to acknowledge my committee members, Dr. Goutam Koley, Dr. William Harrell, and Dr. Apparao Rao for their support and consideration of my work. Especially I would like to recognize my advisor, Dr. Goutam Koley, for his encouragement and constant guidance as I completed my Master's course of study. I have known Dr. Koley since he hired me to work in the NESL as an undergraduate student, and I am grateful for all the lessons and good memories from my time there.

I would also like to thank Dr. Durga Gajula and Dr. Ifat Jahangir for aiding me with their expertise in MEMS fabrication and SEM imaging. The devices used throughout my research were fabricated and imaged by their hard work. This work was financially supported by the National Science Foundation through Grants: IIP-1512342, IIP-1602006 and ECCS-1809891. The fabrication of the microcantilevers was performed at the Georgia Tech Institute for Electronics and Nanotechnology, a member of the National Nanotechnology Coordinated Infrastructure, which is supported by the National Science Foundation (Grant ECCS-1542174).

I would like to express my appreciation for my senior peers Dr. Soaram Kim, Ferhat Byram, and Digangana Kahn who were always there inside and outside the NESL and willing to help me with whatever I needed. I would also like to thank some undergraduate students who aided in my research including Robert Irvine, Harrison Eggers, and Zane Odeh.

Finally, I would like to acknowledge my mother, father, and sister for their love and support throughout my academic journey, I could not have done it without you.

TABLE OF CONTENTS

	Page
TITLE PAGE	i
ABSTRACT.....	ii
DEDICATION	iv
ACKNOWLEDGMENTS	v
LIST OF TABLES	viii
LIST OF FIGURES	ix
CHAPTERS	
I. INTRODUCTION	1
Why VOC Sensing.....	1
VOC Sensing Methodologies	2
Applications of MEMS for VOC Sensing	3
AlGaIn/GaN Microcantilever Heater Based Sensing.....	4
II. DESIGN OF SINGLE CHANNEL MICROCANTILEVER	6
Cantilever Geometry.....	6
MATLAB Simulation of Cantilever Parameters	8
Mask Design	10
III. SINGLE CHANNEL MICROCANTILEVER CHARACTERIZATION...	15
Sensor Parameters and IV Characteristics	15
VOC Sensing Setup	16
Response to VOC.....	17
IV. VOC SENSOR SYSTEM DESIGN	21
PCB design.....	21
System Assembly and Response.....	23
IOT System	24

Table of Contents (Continued)

	Page
V. DUAL CHANNEL MICROCANTILEVER HEATERS	29
Breakdown Characterization.....	31
VOC Sensing Results.....	34
VI. TESTING USING FIELD DEPLOYED COMMERCIAL SENSOR SYSTEM	44
Study of Environmental Parameters Triggering Asthma.....	44
Airthinx Data Collection and Analysis	45
VII. CONCLUSIONS.....	49
Summary of Research	49
Future Works	49
APPENDICES	51
A: Code Written for Research.....	51
REFERENCES	56

LIST OF TABLES

Table		Page
2.1	Single Channel Microcantilever Heater Resistances	9

LIST OF FIGURES

Figure	Page
2.1 Cantilever Single Arm Diagram	7
2.2 Cantilever Tip Diagram	7
2.3 Layer structure for GaN on SI 6” wafer purchased for fabrication of Triangular Microcantilever Heaters (TMH) Supplier: NTT Advanced Technology Corporation, Japan	10
2.4 2017 Fabrication Mask Layout in AutoDesk 360.....	11
2.5 Close up of the fabrication mask for geometries SS1 and SS2.....	12
2.6 Transmission Line Measurement (TLM) test results and trendline	13
2.7 Sheet resistance mapping over whole wafer from manufacturer.....	14
3.1 Optical image of a device with geometry SS1	15
3.2 (a) IV characteristics and resistance of a typical SS1 geometry (b) SS2 geometry	15
3.3 Diagram of the VOC sensing setup used in all experiments	17
3.4 Response of a single channel microcantilever (SS1) at 20V to 50,000 ppm of isopropanol, methanol, and acetone for a duration of 15 s.....	18
3.5 Individual slope test results for isopropanol.....	19
3.6 Average slope of the current response to three VOCs of varying concentrations	19
4.1 EAGLE CAD PCB design with (1) power routing, (2) transimpedance amplifier, (3) Op Amps, (4) Voltage regulator, and (5) LCD control	22
4.2 Portable VOC sensing system final assembly	23

List of Figures (Continued)

Figure	Page
4.3 Percent change of voltage on the ADC pin of the Arduino in Prototype in response to 25,000 ppm VOC vapor	24
4.4 IoT System Schematic, (a) VOC Sensor, (b) transimpedance amplifier, (c) ADC expansion board, (d) Raspberry Pi 3, (e) Amazon IoT and DynamoDB, (f) graphical output	26
4.5 (a) VOC Sensor, (b) transimpedance amplifier, (c) ADC expansion board, (d) Raspberry Pi, (e) Monitor Display.....	27
4.6 Data from DynamoDB showing sensor response to isopropanol.....	28
5.1 SEM Image of several dual channel microcantilevers.....	29
5.2 (a) SEM image of a monolithic tip dual channel microcantilever heater (MDC-MH), Ti/Au contacts, and substrate (b) SEM image showing the two parallel AlGaN channels and the gap distance at the tip.	30
5.3 Resistance curves of the inner and outer channel below the breakdown voltage	31
5.4 (a) Breakdown I-V characteristic of a monolithic tip dual channel microcantilever heater (MDC-MH) when 1 V is applied to the outer channel (b) Schematic of the currents in a MDC-MH at pre-breakdown and post-breakdown voltage biases.	32
5.5 Breakdown current in the outer channel with 0V applied to the outer channel with line indicating the crossing of the 1 μ A threshold and the breakdown voltage indicated by VB.	33
5.6 Current in the outer channel while in the inner channel is swept past breakdown in the presence of either neutral gas, acetone, methanol, or isopropanol.	

	Inset: Close-up emphasizing the different zero-crossing point voltages of the different VOCs. Inset Table: Latent heat of evaporation (ΔH_{vap}) of relevant VOCs.	35
5.7	V _{zc} values for 25,000 ppm isopropanol for six different sample cantilevers (SC)	36
5.8	SC1000 Infrared microscope	37
5.9	(a) Optical image of monolithic tip dual channel microcantilever heater (MDC-MH) (b) Infrared microscopy image of MDC-MH under pre-breakdown bias conditions (c) Infrared microscopy image of MDC-MH during breakdown.	38
5.10	Current at all four terminals of a monolithic dual channel microcantilever heater (MDC-MH) when isopropanol is introduced at 15 sec. to induce breakdown until the system is purged with clean air at 40 s	40
5.11	Breakdown current ($I_{o1} + I_{o2}$) in response to 25,000 ppm isopropanol.....	41
5.12	Amplification factor of the breakdown current ($I_{o1} + I_{o2}$) relative to the initial current pre-breakdown $(I_{o1} + I_{o2})_0$	41
5.13	(a) Current at all four terminals of a monolithic dual channel microcantilever heater (MDC-MH) when methanol is introduced (b) acetone	42
6.1	Airthinx air quality monitoring system.....	44
6.2	Map of deployed Airthinx systems	45
6.3	Example of the weekly variation of formaldehyde (CHO ₂).....	46
6.4	Example of the weekly variation of PM ₁₀	46
6.5	Weekly averages of formaldehyde (CHO ₂) for a single patient.....	47
6.6	Weekly averages of PM ₁₀ for a single patient	47

CHAPTER ONE

INTRODUCTION

Why VOC Sensing?

Volatile organic compounds (VOCs) describe a wide class of organic compounds that are known for their high vapor pressure and low solubility in water. Members of this classification include alkenes, alkanes, alcohols, aromatic hydrocarbons etc. and are not limited to any one subgroup of organic compounds. Some more notable VOCs that concern human health include formaldehyde, benzene, toluene, chloroform, and acetone [1-2]. Vapors from these solvents can be absorbed through the skin, lungs, and other orifices. While VOCs are mostly naturally occurring chemicals, when exposed to unnatural concentrations the health effects in humans are clearly seen. With so many types of VOCs a wide and varied range of medical issues arise, but among the most concerning are asthma, neurological problems including depression, and cancer. Due to factory processes of commercial products such as furniture, carpeting, paints, and electronics our indoor environments are constantly being inundated with outgassing VOCs. With the addition of VOCs from cleaning products, adhesives, and cooking methods there are over 900 different types of VOCs detectable in indoor spaces. Furthermore, the concentration of VOCs is typically 5 to 10 times higher than it is outdoors, which can be amplified in urban environments [3-5]. Because of increasing time spent indoors by humans and ongoing urbanization, VOCs pose a modern health problem that needs to be addressed from all sides. Long term solutions include change in factory processes, switching to all-natural cleaning products, and equipping indoor spaces

with quality filtration systems, but unfortunately, they are impractical in the short term. A more effective immediate measure would be to identify sources of large concentrations of especially harmful VOCs and remove them from our indoor environments. Identification can be aided by electrical sensing equipment, and there are several technologies for doing so. However, to be truly impactful on a wide scale, the sensing technology needs to be sensitive, selective, portable, and inexpensive.

VOC Sensing Methodologies

Current technologies for VOC detection can be separated into two categories: non-selective and selective. Non-selective VOC sensing mechanisms are well established and generally can detect VOCs down to the ppm and ppb range. Photo Ionization Detectors (PID) and Flame Ionization Detectors (FID) are commonly used by environmental agencies and health inspectors to help assess overall air quality. These technologies rely on the ionization of organic compounds by either a hydrogen-air flame (FID) or UV radiation (PID), and collection of these ions on electrodes which produces a current [6], [7]. While effective at measuring VOC concentration, PIDs and FIDs often cost several thousand dollars and are unable to identify specific VOCs. Cheaper and more widespread VOC sensors are hot bead pellistors and chemiresistors. These technologies typically utilize a Wheatstone bridge configuration with one branch as the sensor. The hot bead pellistor combusts VOCs and the exothermic reaction causes a measurable change in resistance, while chemiresistors change resistance with the chemisorption of VOC molecules [7]. The main technology used for selective detection and identification of

VOCs is spectrometry. Mass spectrometry and Ion-mobility spectrometry operate by separating molecules by their mass and/or ionic charge and can give the user the exact chemical composition of any sample VOC or otherwise [8]. Despite its advantages, spectrometry machines are expensive non-portable. None of the traditional VOC sensing technologies have all the attributes required for effective change indicated at end of the previous section. Micro Electrical Mechanical System (MEMS) based sensors, however, are good candidates to meet those requirements and are discussed in the next section.

Applications of MEMS for VOC Sensing

Because of the health risks associated with VOCs and the apparent gap in technology for their sensitive, selective, portable and inexpensive detection, there are many groups utilizing the gamut of MEMS devices to try to meet the demand. Non-selective VOC detection has been shown with gateless HFETs, branch-like NiO/ZnO heterostructures, and polymer cantilevers [9-11]. Selective VOC detection with MEMS typically involves the use of functionalization, which are often spray coated polymers. Examples of functionalized devices include AlN/SiO₂/Si Surface Acoustic Wave (SAW) devices, polymer coated diamond and silicon microcantilevers, and Capacitive Micromachined Ultrasonic Transducers (CMUT) with various polymer coatings [12-14]. The inherent problem with functionalized devices is that their performance diminishes over time with the degradation of the functionalization layer. Non-functionalized yet selective VOC sensing has been shown with AlGaIn/GaN microcantilever heaters, which will be discussed in further detail in the next section.

AlGa_N/Ga_N Microcantilever Heater Based Sensing

Microcantilevers with heater elements were originally devised in the late 1990s for thermomechanical data writing by forming nanoscale deformations in polymers using heated Si tips [15]. The silicon based microcantilever heaters were often used in conjunction with an atomic force microscope (AFM) utilizing its fine motor control that was necessary for many other applications including nanoscale topography imaging and deposition processes [16] - [17]. A heated cantilever based nanotopographical sensor demonstrated earlier [18] had four terminals where the outer channel was a heater, and a thermally and electrically isolated piezoresistive inner channel was used for enhanced nanotopographical sensing. The hybrid device was fabricated from single crystalline silicon and had doped silicon traces because the melting point of silicon (1412 °C) is higher than most metals used for traces, allowing for high current/temperature operation without electromigration [18]. However, an AlGa_N/Ga_N heterostructure has a melting point of 2500°C and requires no doping to form a conductive channel.

III-Nitride semiconductors are well known for their application in high power microwave and power electronic devices owing to their large band gap and unique polarization properties that results in the formation of high sheet charge density and carrier mobility at heterostructure interfaces [19] - [21]. In recent years, with the availability of high quality III-Nitride epitaxial layers on Si substrate, there has been a renewed focus on developing III-Nitride based microelectromechanical systems (MEMS) taking advantage of their unique material properties. [22] – [23]. Polarized III-Nitride surfaces have a propensity to interact with polar molecules, a property that has been exploited to develop

gateless III-Nitride heterostructure field effect transistors (HFETs) with exposed gate areas, which allow polar molecules to alter the 2DEG upon adsorption. These FET type sensors have shown success in sensing aqueous salts, nitrous oxide, and volatile organic compounds (VOCs) [9], [24]. In recent years, piezoresistive and piezotransistive microcantilevers fabricated from this material system have been used for highly sensitive detection of displacement, trace explosives, surface potential, acoustic waves, and volatile organic compounds (VOCs) [25] – [30]. Due to their highly polar surface and presence of a sub-surface electronic sheet charge of high density and mobility, AlGaN/GaN heterojunction based triangular microcantilevers are inherently suitable for integrating heater channels and developing low power sensors for detecting VOCs [28] – [30]. This has been explained by considering VOC condensation in the surrounding region of the tip followed by rapid transport (induced by convection) and re-evaporation closer to the tip, removing latent heat and lowering the tip temperature [29]. Two types of TMH based VOC sensors have been investigated so far; one with a single combined heating and sensing channel [28], and the other with an outer sensing channel and a separate inner heating channel, which also demonstrated the capability to identify individual components in a VOC mixture [30]. However, the change in device signal in presence of VOCs was generally <5%, and the limit of detection was found to be in the ppm range [14]. A sensitivity down to ppb range is typically required to ensure widespread applicability of VOC sensors [6], [31].

CHAPTER TWO

DESIGN OF CANTILEVER HEATER SENSOR

Cantilever Geometry

Triangular microcantilever heaters (TMH) are designed to maximize the temperature at the tip of the cantilever with lowest power input. As a MEMS device power consumed is a key component to the applicability of the sensors in real world systems. Because of the 2DEG created at the AlGa_N/Ga_N heterojunction with a sheet carrier density on the order of $10^{13}(\text{cm}^{-2})$ the resistivity of these micrometer thick cantilevers is low enough to allow enough current for self-heating. Joule heating is proportional to the power consumed and thus current should be maximized over resistance since the heating depends on the square of the current. The major source of lost power in TMHs is related to the thermal conductivity of the arms removing heat from the tip region [29]. Wider arms allow for more current and more heat conduction but also increase the thermal mass of the cantilevers allowing more heat to be contained in the system. Many different geometries have been attempted for AlGa_N/Ga_N microcantilevers that were unsuccessful at sensing VOCs, the most successful have been simple triangular shaped cantilevers that had tapered arms and a slightly rounded tip with a width of approximately $3\mu\text{m}$. The initial resistance of the arms for this basic shape for any variation in width and path length can be determined by Equation 1.1.

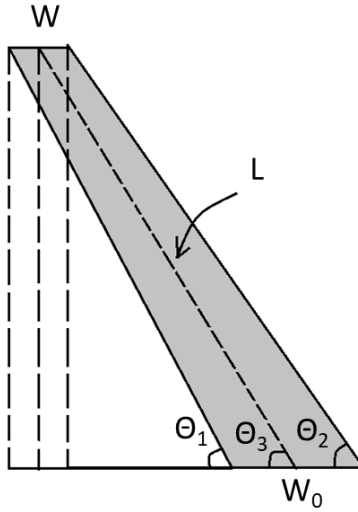


Figure 2.1: Cantilever Single Arm Diagram

$$(1.1) R_{arm} = RS * \int_0^L \frac{dL}{W_0 - 2(L \cos(\theta_3) - L \sin(\theta_3) \cot(\theta_2))}$$

Where RS is the sheet resistance of the AlGaIn/GaN, L is the length of the bisecting path, and θ_3 and θ_2 are the angles shown in the diagram (Fig. 2.1). The resistance tip of the cantilever can be estimated by considering a rainbow shaped conductor with many parallel paths as shown by Equation 1.2.

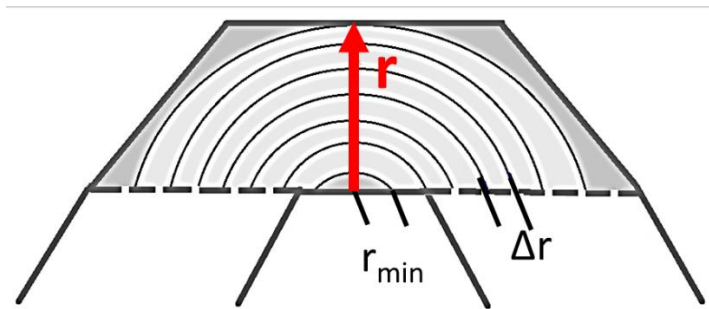


Figure 2.2: Cantilever Tip Diagram

$$n = r_{min} : \frac{r}{\Delta r} : r$$

$$L_n = \pi r_n \quad W = \Delta r$$

$$R_n = RS * \frac{L_n}{W}$$

$$(1.2) R_{tip} = \frac{1}{\frac{1}{Rrmin} + \frac{1}{Rn} \dots + \frac{1}{Rr}}$$

Where n is the number of paths, L_n is the length of each path, Δr is the width of each path, R_n is the resistance of each path, and R_{tip} is the parallel resistance of the paths and the total resistance of the tip. The smaller Δr becomes the closer the result will be to the theoretical value of the tip resistance. For future designs of TMHs this mathematical model can aid in deciding the dimensions if certain boundaries are set on the parameters to take into consideration the conduction losses, structural integrity, and fabrication limitations.

MATLAB Simulation of Cantilever Parameters

Utilizing the equations in the previous section a MATLAB program was written to confirm the validity of the theoretical resistances compared to preexisting TMHs, the code can be found in Appendix A. The preexisting TMHs were of three types A, B, and C but geometrically similar, so the theoretical resistances are the same. Type A has a total base of 220 μm , arm base of 60 μm , and height from substrate of 280 μm . The measured resistance values of the cantilevers from three different chips are shown in Table 2.1.

Cantilever Type		Chip 1			Chip 2			Chip 5			Average Resistance
A	Measured Resistance (Sheet Resistance)	15.2k Ω (420)	17.5k Ω (480)	18.3k Ω (510)	13.8k Ω (380)	14.2k Ω (390)	16k Ω (440)	12.9k Ω (360)	13.6k Ω (380)		15.6 k Ω
B	Measured Resistance (Sheet Resistance)	12.1k Ω (340)	15k Ω (420)	15.3k Ω (420)	13.2k Ω (370)	14.3k Ω (400)		13k Ω (360)	14.6k Ω (400)		14.2 k Ω
C	Measured Resistance (Sheet Resistance)	14.6k Ω (400)	15.6k Ω (430)	16.5k Ω (460)	12.2k Ω (340)	13.2k Ω (370)		14.3k Ω (400)			14.9 k Ω
Average Measured Resistance (Average Sheet Resistance)		15.6k Ω (430)			13.8k Ω (380)			13.7k Ω (380)			Average of all cantilevers 14.5kΩ

Table 2.1: Single Channel Microcantilever Heater Resistances

The average resistance of all the cantilevers was found to be 14.5 k Ω , and the range was from 12.1 k Ω (-16.6%) to 17.5 k Ω (+20.1%). Using the TLM measured sheet resistance of 354 (Ω /square) the MATLAB program determined the theoretical resistance of this shape of TMH to be 11.1k Ω . The measured resistance of the cantilevers is predictably higher than the pure geometrical simulation because of the stress induced on the material once it is released from the substrate, also the actual width of the AlGaIn channel (conduction path width) can be slightly less than the GaN beneath it because of over etching. Therefore, a correction factor of 1.3 was added to the simulation to account for these differences, derived from the factor of increase from simulated to measured result. The tips of the cantilevers have a radius of 3 μ m and MATLAB was used to find the theoretical tip resistance by using very small values of Δr from Equation 2.2, in the limit for a sheet resistance of 354 (Ω /square) tip resistance was determined to be 423 Ω .

Next the program was updated to aid in the design of new cantilevers. Because the goal of the design is to minimize power consumed while achieving adequate heating

at moderate bias voltages, the resistance of the devices would preferably be minimized. However, the geometry of the tip should adhere to a previously proven design to ensure that enough Joule heating for sensing occurs at that location. The MATLAB program is written to vary the initial arm width, total base width of the TMH, and height from substrate to tip within certain boundaries to account for all arm lengths and angles in the design space. Then if the overall resistance of the cantilevers is within a preset range the program will return the geometrical parameters, this code can be found in Appendix A. From the results of the program two new low resistance geometries of TMH were chosen to be included in a new fabrication mask.

Mask Design

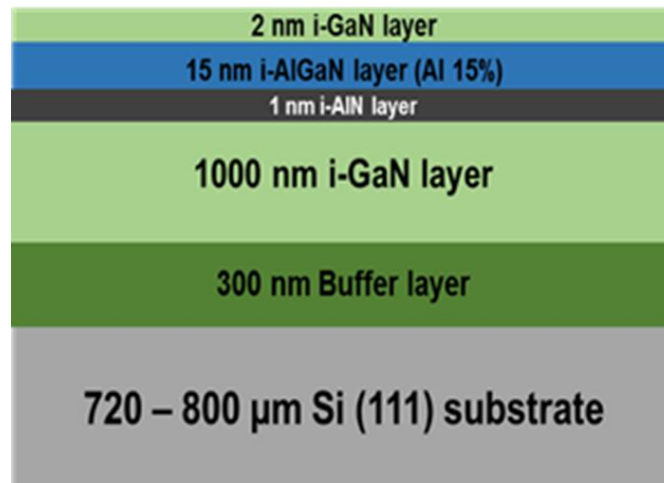


Figure 2.3: Layer structure for GaN on Si 6" wafer purchased for fabrication of Triangular Microcantilever Heaters (TMH) Supplier: NTT Advanced Technology Corporation, Japan

The TMHs used in this study were fabricated using AlGa_N/Ga_N epitaxial layers grown on a 625 μm thick Si (111) substrate, purchased from NTT Advanced Technology Corporation, Japan. The wafers had a 2 nm i-GaN cap layer and 15 nm Al_{0.25}Ga_{0.75}N on

top of 1 μm i-GaN, with a 300 nm buffer layer separating the GaN layer from the thick Si substrate. At the beginning of the fabrication process, the top 100 nm of AlGaIn/GaN layer was etched using BCl_3/Cl_2 plasma to isolate the cantilever mesa, followed by another deep etch to define the cantilever geometry. Then Ti(20 nm)/Al(100 nm)/Ti(45 nm)/Au(55 nm) metal stack was deposited and followed by a rapid thermal annealing process at 825 $^\circ\text{C}$ for one minute, to form the ohmic contacts on the mesa region. Ti(20 nm)/Au(225 nm) stack was deposited afterwards to form the probe contacts. Finally, Bosch process was used, with plasma-enhanced chemical vapor deposited SiO_2 masking layer at the backside, to perform through wafer etching of the silicon layer to release the cantilevers. The masks were first rendered in AutoCAD 360 and the mask used for the cantilevers fabricated in 2017 is shown in Fig. 2.4.

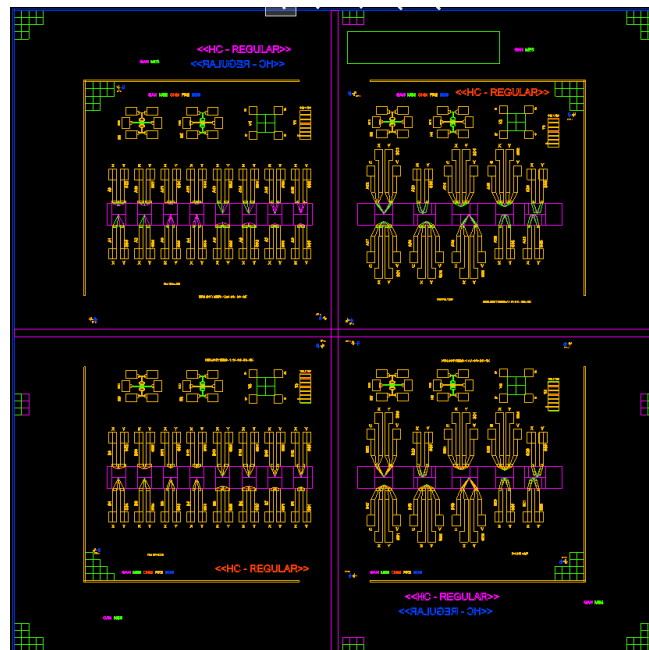


Figure 2.4: 2017 Fabrication Mask Layout in AutoDesk 360

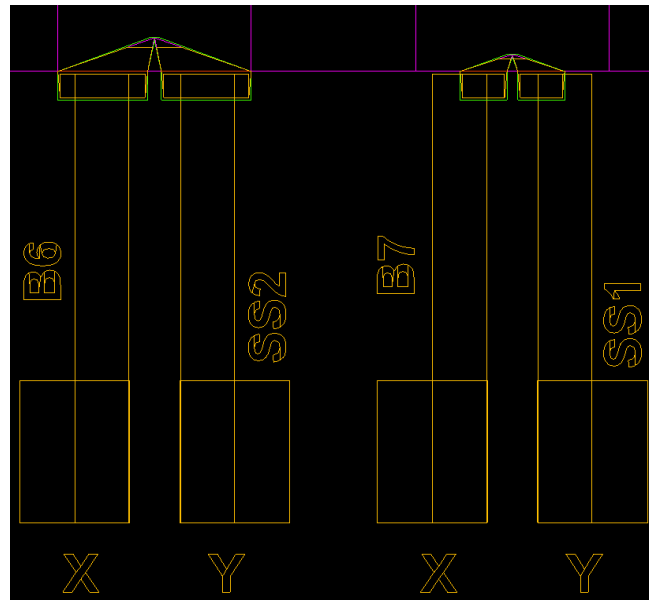


Figure 2.5: Close up of the fabrication mask for geometries SS1 and SS2

Two of the cantilever designs in the mask were derived directly from the MATLAB simulation for resistance minimization, and they are shown in detail in Fig. 2.5. The geometry SS1 had a total base of $214\ \mu\text{m}$, an arm base of $96\ \mu\text{m}$, and height from substrate to tip of $35\ \mu\text{m}$. The geometry SS2 had a total base of $396\ \mu\text{m}$, arm base of $184\ \mu\text{m}$, and height of $70\ \mu\text{m}$. Both cantilevers were predicted to have a resistance of around $3\text{k}\Omega$ at a sheet resistance of $354\ (\Omega/\text{square})$. However, the AlGaIn/GaN wafer purchased from NTT Advanced Technology Corporation, Japan for this fabrication had a higher sheet resistance than the one used for the previous cantilevers. After the new fabrication the sheet resistance could be determined from the Transmission Line Measurement (TLM) test pattern than was deposited on the wafer. The resistance was measured between the subsequent gaps in the AlGaIn/GaN of $10, 15, 20, 25,$ and $30\ \mu\text{m}$, to create a trendline from which the resistance data could be extracted. The TLM contacts were wire

bonded on a dual in line package chip carrier and the results of the TLM data are shown in Fig. 2.6

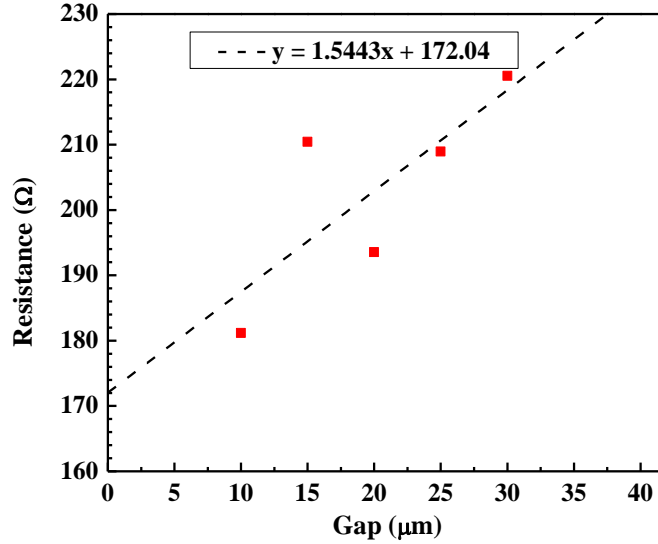


Figure 2.6: Transmission Line Measurement (TLM) test results and trendline

The y-intercept of the trendline is equal to twice the contact resistance, in this case each contact resistance was $\sim 86 \Omega$. The slope of trendline can be used to determine the slope based on the formula below, and the known TLM pattern width was $300 \mu\text{m}$.

$$Slope = \frac{R_S}{W} \rightarrow R_S = (1.5443)(300) = 463.3 \left(\frac{\Omega}{\square}\right)$$

This measured sheet resistance matches closely with the non-destructive sheet resistance mapping over whole wafer from manufacturer, shown in Fig. 2.7. With this new sheet resistance, a more accurate simulated resistance could be determined for the geometries SS1 and SS2, and they were $3.5 \text{ k}\Omega$ and $3.9 \text{ k}\Omega$ respectively. Now that the fabrication was complete the devices could be characterized and tested for sensitivity to VOCs.

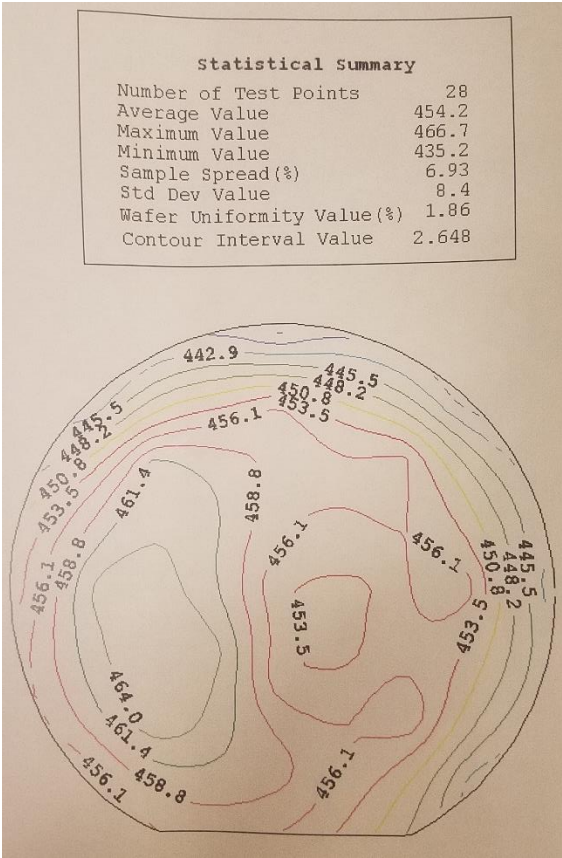


Figure 2.7: Sheet resistance mapping over whole wafer from manufacturer

CHAPTER THREE

SINGLE CHANNEL MICROCANTILEVER CHARACTERIZATION

An optical image of a TMH with the geometry SS1 is shown in Fig. 3.1, upon inspection the fabricated cantilever matches accurately with mask design.

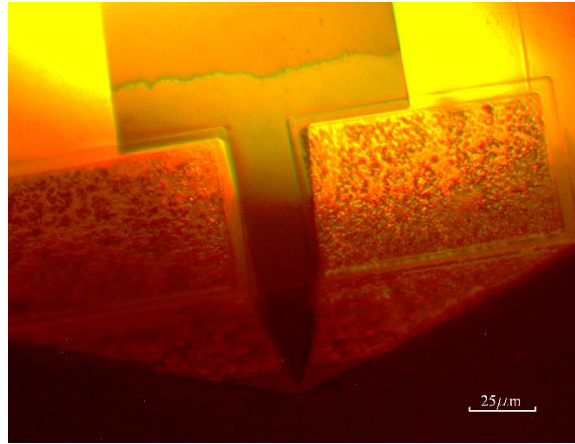


Figure 3.1: Optical image of a device with geometry SS1

Sensor Parameters and IV Characteristics

Using an Agilent B2900 SMU the IV characteristics for the geometries SS1 and SS2 were determined under dark closed chamber conditions, the results are shown in Fig.

3.2.

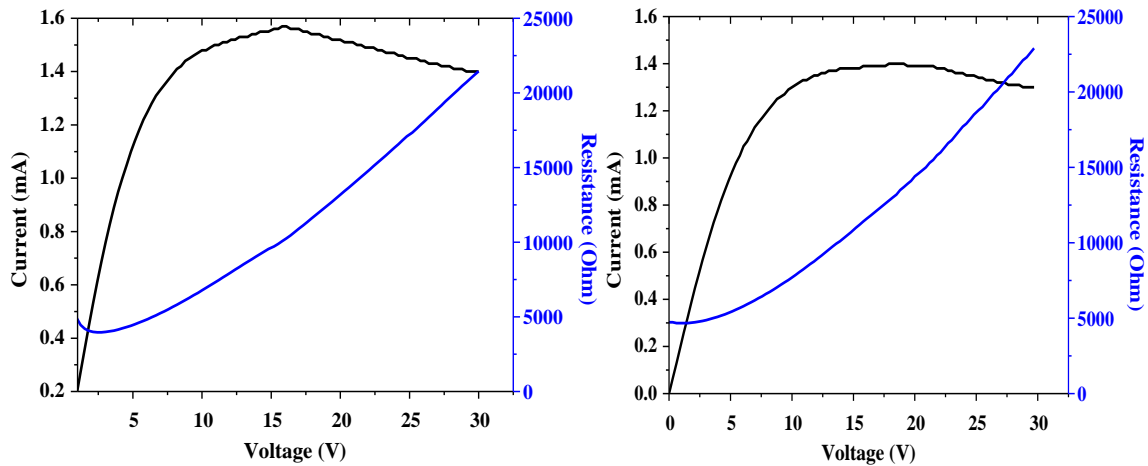


Figure 3.2: (a) IV characteristics and resistance of a typical SS1 geometry (b) SS2 geometry

Initially the IV curve is linear as expected for any normal resistor, but once the voltage reaches around 7.5 V noticeable self-heating begins in the microcantilevers. The geometry SS1 reaches a maximum current at around 16V while SS2 peaks at 17.5 V, this indicates suitability for operation at a constant bias of under 20V. The actual resistance of the devices can be determined from the minimum of the resistance curve, for this SS1 device the resistance is 4.5 k Ω , while the SS2 is 4.9 k Ω . Although the measured resistance values are around a 1 k Ω higher than the simulated values they are still within the expected margin of error for fabricated devices and are roughly three times less resistive than the previous TMH design. With characterization complete the TMHs can be tested for sensitivity to VOCs.

VOC Sensing Setup

Calibrated VOC vapors can be produced by taking saturated VOC vapor, which has a known concentration at the ambient temperature and diluting it with pure Nitrogen gas. The three VOCs employed in this study were isopropanol, methanol, and acetone because of their wide range of latent heat of evaporation, availability, and relatively smaller health risks when compared to other VOCs. The setup that was used to produce the calibrated gases is shown in Fig. 3.3.

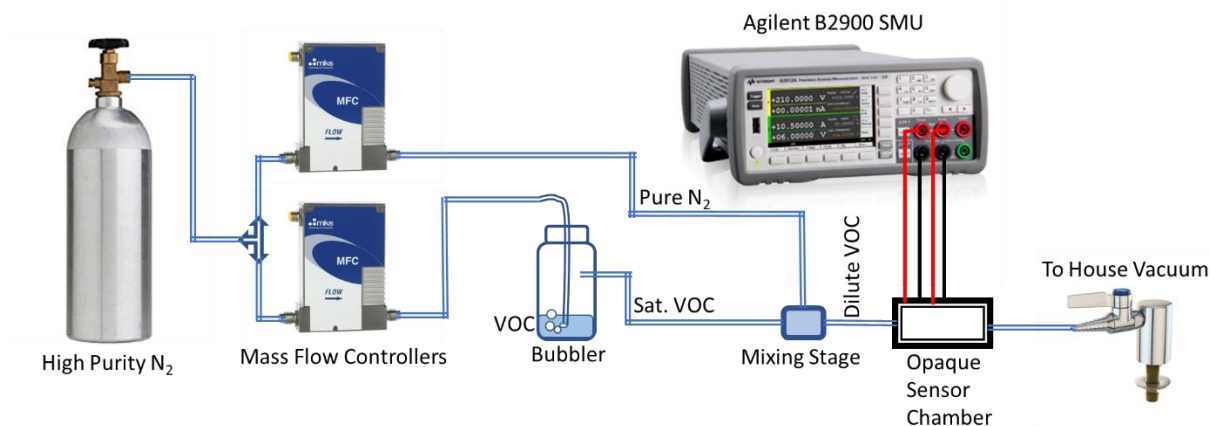


Figure 3.3: Diagram of the VOC sensing setup used in all experiments

High purity N_2 was flown through two mass flow controllers (MFC) with a maximum flow rate of 2000 sccm. One of the MFCs lead to a bubbler containing a VOC and saturated VOC vapor in the headspace, which then flowed out to a mixing stage. The other MFC flowed pure N_2 to the mixing stage to create the calibrated VOC vapor concentration. From the mixing stage the calibrated gas flowed into an airtight and opaque container which housed the sensor and wiring connections to Agilent B2900 SMU. To ensure continuous airflow, the outlet of the sensor chamber led to the house vacuum set low enough to be insignificant compared to the airflow from the MFCs. The vacuum could also be raised once the VOC vapor was cut off for a quick purge of the sensor chamber allowing for fall time measurements and rapid testing.

Response to VOC

Using the testing setup in the previous section the new TMH devices could be tested for their response to known concentrations of VOCs. Diluted VOC was flown into the sensor chamber shortly after the device was turned on and lasted for approximately 15

s until the air through the bubbler was turned off and pure N₂ filled the sensor chamber. The current response of a SS1 geometry device biased at a constant 20 V to the three different VOCs at a concentration of 50,000 ppm is shown in Fig. 3.4.

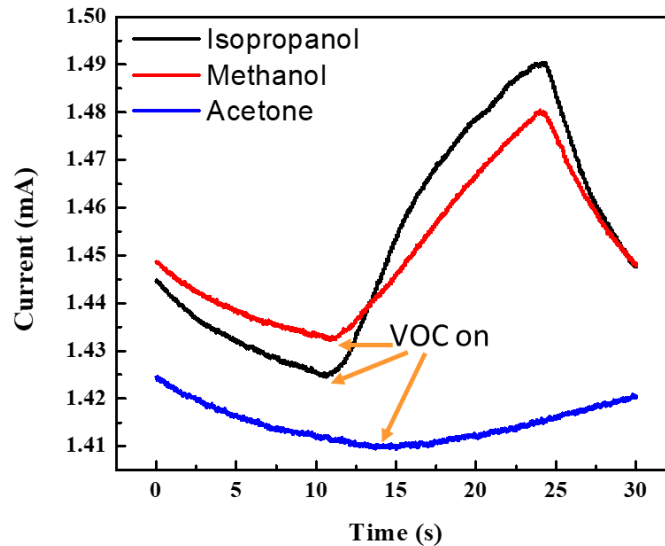


Figure 3.4: Response of a single channel microcantilever (SS1) at 20V to 50,000 ppm of isopropanol, methanol, and acetone for a duration of 15 s

Within the 15 second window the device experienced a 4.3% increase in current in the presence of isopropanol, 3% increase for methanol, and 0.7% increase for acetone. The reduction in current in the first 10 seconds of the experiments can be attributed to continual device heating at the bias voltage, this drift would continue for several minutes after the device was turned on, but in the interest of preserving the cantilevers the exact duration was not measured. The important parameter for making a practical sensing system from these devices is the slope of the current response to the different VOCs. The slope response was tested for this SS1 TMH over the range from 25,000 – 50,000 ppm and the results for isopropanol are shown Fig. 3.5. Within this range of concentrations,

the slopes of the current response remain consistent. Although the baseline of the sensor changes slightly from experiment to experiment this does affect the slope.

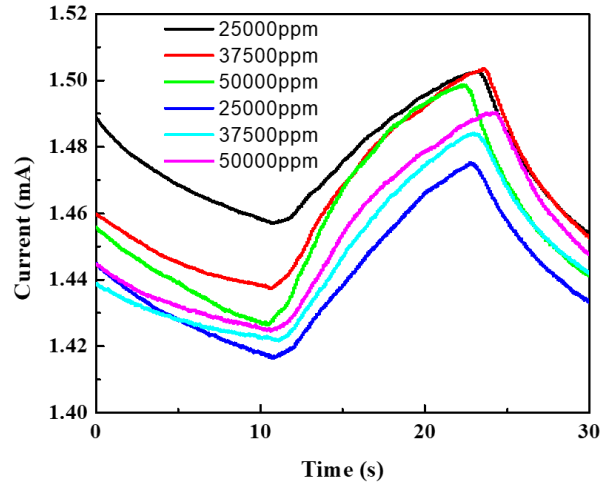


Figure 3.5: Individual slope test results for isopropanol

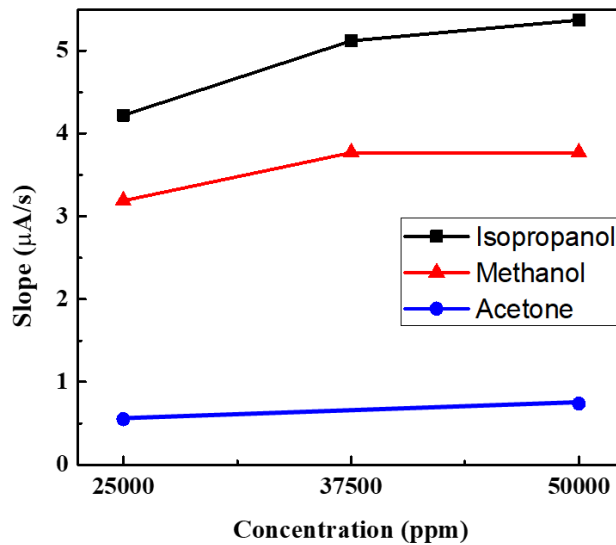


Figure 3.6: Average slope of the current response to three VOCs of varying concentrations

The average slope was determined from the minimum and maximum points of the current response to the VOCs, which corresponds to beginning and end of the VOC vapor

flow to the sensor. As shown in Fig. 3.6, within the range of tested concentrations, the slope of the response could be used to differentiate between the three analytes.

Furthermore, the differences magnitude of the slope response of the different VOCs correlate directly with their different latent heats of evaporation (ΔH_{vap}). Isopropanol has the highest ΔH_{vap} and steepest slope response, acetone has the lowest ΔH_{vap} and shallowest slope, and methanol is between the other two in both cases. Because this result could be achieved at a moderate bias voltage of 20V and consumed approximately 30mW of power a portable VOC sensing prototype was proposed and constructed and is discussed in the next section.

CHAPTER FOUR

VOC SENSOR SYSTEM DESIGN

As previously stated VOCs pose an ever-increasing health risk to humans. To combat this issue a plethora of IoT air quality monitoring devices have been created (such as Flow by Plume Labs or the Cub by Ion), which pack an impressive amount of sensing capability into a small package. However, these technologies can only detect that a VOC is present and therefore guess at concentration with no discernment between compounds [32]. As the US market for indoor air quality monitoring is expected to reach \$12.2 billion by 2023 there is adequate demand for improvement of the technology. [33]. The VOC sensing system devised in this work was designed with several key factors in mind. The system had to be portable and therefore be powered with readily available and preferably rechargeable batteries. By using a reprogrammable micro controller, the system would have the flexibility needed for prototyping and rapid upgrades. A small DC fan could be used to control the airflow into the system. A low power LCD screen could be used to relay real time VOC information to the user.

PCB Design

The first step in designing the portable prototype was to choose a micro controller with good versatility and low power requirements. The classic Arduino Uno was a good fit for the application and provided the computing power for the rest of the system to operate. For a compact design an Arduino shield PCB was designed in EAGLE CAD to interface between the micro controller and the rest of the system. The EAGLE CAD rendering of the board is shown in Fig. 4.1.

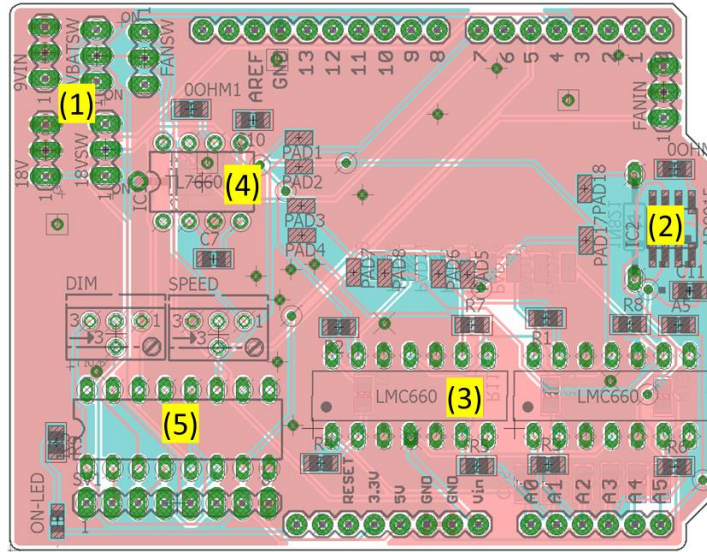


Figure 4.1: EAGLE CAD PCB design with (1) power routing, (2) transimpedance amplifier, (3) Op Amps, (4) Voltage regulator, and (5) LCD control

The PCB is designed to route power (1) from the batteries to microcontroller, sensor, LCD, and fan including switches to turn the various components on and off. The next important function of the PCB is to convert the VOC sensor current to a voltage that could be read by the Arduino Uno ADC. This is accomplished by using a transimpedance amplifier [AD8015 (2)] to accurately convert the signal to a voltage and a non-inverting amplifier through LMC660 Op Amps (3) to amplify the signal to an appropriate voltage. The Op Amps are provided voltage on their negative terminal by a TL7660 CMOS Voltage Converter (4). Also included is an IC (5) to write to the LCD from the microcontroller using SPI protocol. The gap in the upper right portion of the PCB is space to mount a microcantilever array chip with contacts so that multiple TMHs can be used at the same time.

System Assembly and Response

The prototype casing was printed using a Zmorph 3D printer. A 7 V rechargeable lithium ion battery is used to power the majority of the components in the assembly, and two 9 V batteries in series provide the voltage required to operate the TMH. A small DC fan blows air out of the backside of the system while pulling air in through airflow inlet tubing. The final assembly is shown in Fig. 4.2.

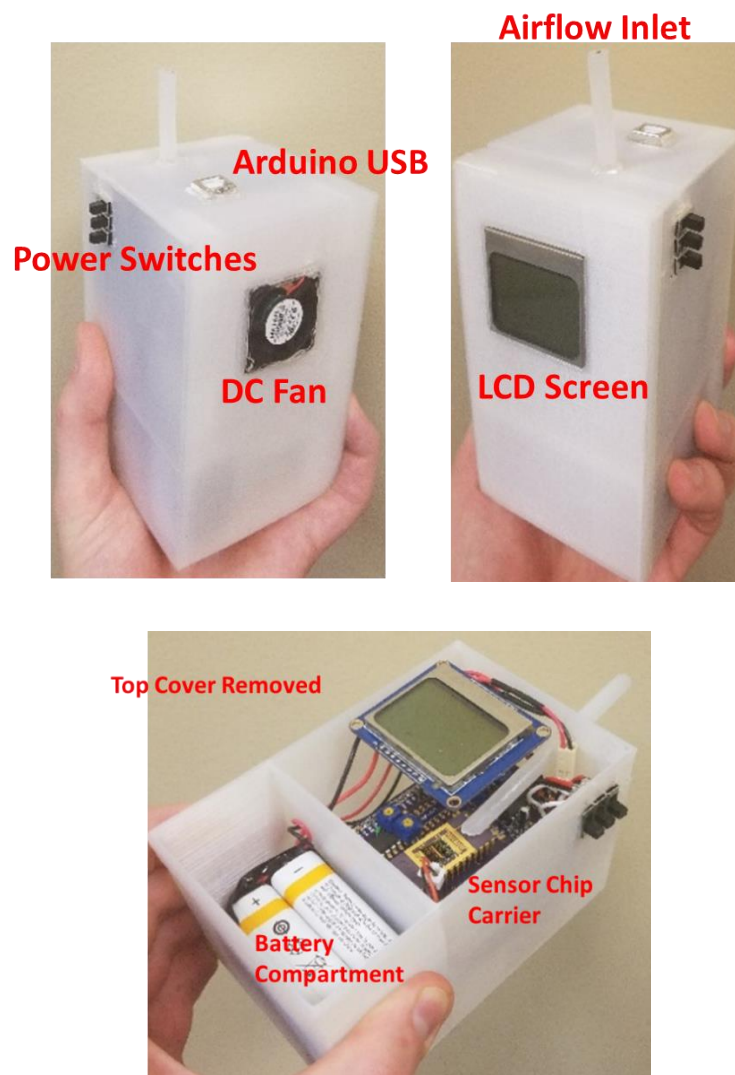


Figure 4.2: Portable VOC sensing system final assembly

The Arduino program used to operate the system accomplished several tasks, including successfully reading sensor data on the ADC, recognizing a change in the slope of the sensor input, and determining that a VOC is present and displaying that information to the user on the LCD screen. However, due to the step-like response to VOCs as shown in Fig. 4.3 the identification of VOCs based on their slope is still under development. The potential of the sensor system is apparent upon inspection of Fig. 4.3 which shows the percentage change from the baseline of values recorded by the Arduino in response to 25,000 ppm of the three analytes. The code written for this stage of the prototype is included in Appendix A.

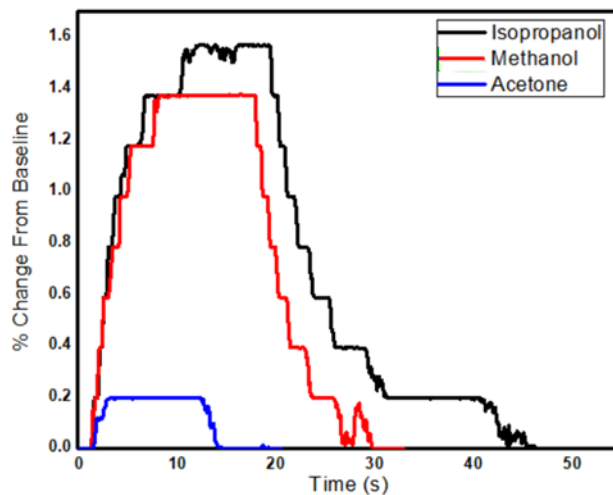


Figure 4.3: Percent change of voltage on the ADC pin of the Arduino in Prototype in response to 25,000 ppm VOC vapor

IOT System

The next stage in the portable sensing project was to develop a system that could be connected to WIFI and be accessed by a computer at another location. Thus, data from

the sensors can be uploaded to an online database. Initially, commercial product research was conducted to find a WIFI enabled microcontroller that could handle the demands of sensor interfacing. A microcontroller with a fast sample rate, high ADC precision, and versatility for handling multiple various sensors was necessary. It was found in the Raspberry Pi 3 combined with a high precision AD/DA expansion board that had 30kHz sample rate, 24-bit resolution capability, and 8 channels. The Raspberry Pi has its own operating system which allows it to be a fully independent base of the IoT system. The microcontroller was programmed to communicate with the expansion board which was then calibrated to ensure an accurate reading. In the initial part of developing of the sensor platform, an enclosure for the wire-bonded sensor chip carrier with calibrated vapor flow capabilities, was fabricated Fig 4.4(a). An inexpensive and readily available online resource was needed to receive and store data online from the WIFI connected microcontroller. Amazon web services (AWS) provided a low-cost option for access to basic cloud tools that could meet our needs, a schematic of the IoT system is shown in Fig. 4.4.

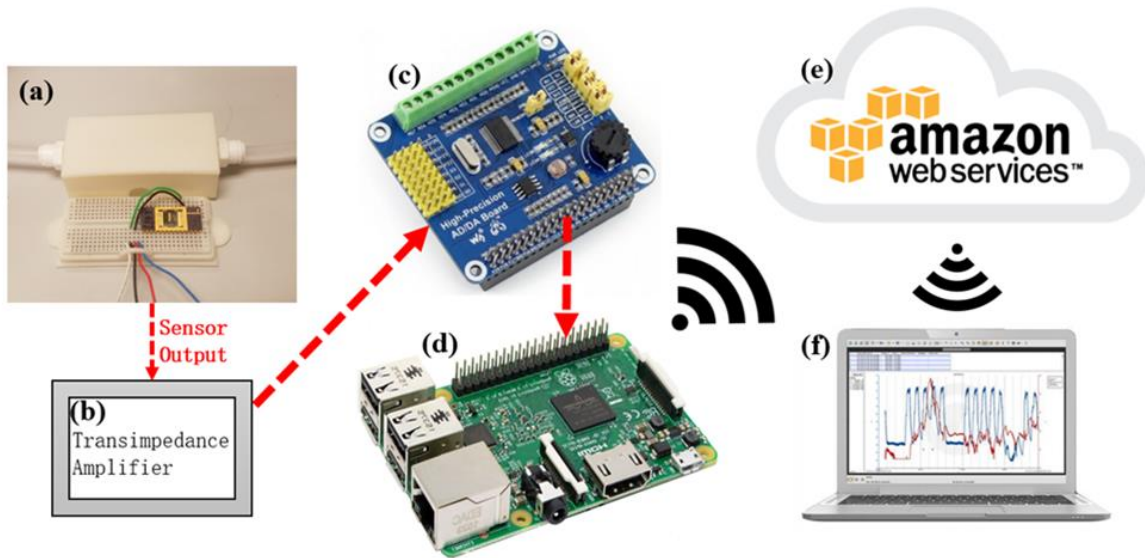


Figure 4.4: IoT System Schematic, (a) VOC Sensor, (b) transimpedance amplifier, (c) ADC expansion board, (d) Raspberry Pi 3, (e) Amazon IoT and DynamoDB, (f) graphical output.

An image of the actual setup in the lab is shown in Fig. 4.5. AWS has many services available depending on the needs of the project. For this project, two of these services: IoT Core and DynamoDB. IoT Core provided a robust and secure framework to allow communication between the cloud and the Raspberry Pi, or any internet enabled device, with APIs available in a variety of languages. Python was utilized the language of choice on the Raspberry Pi, since it was the most versatile and easy-to-read.

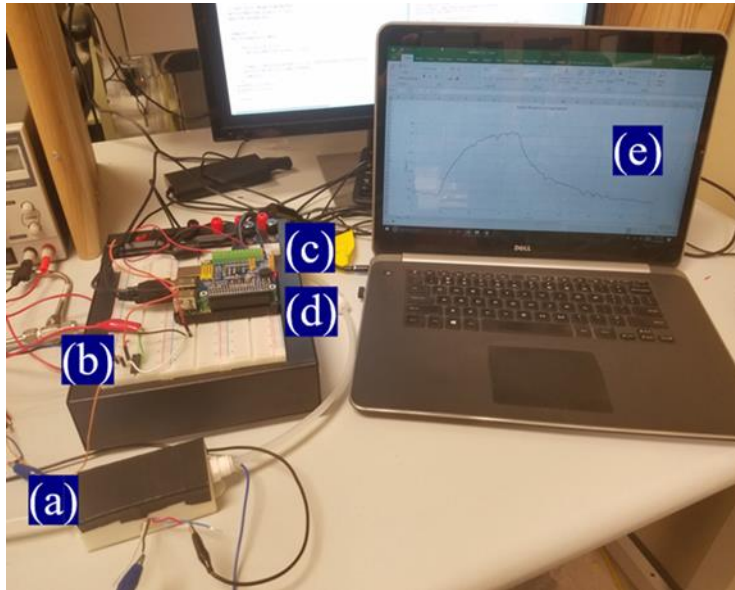


Figure 4.5: (a) VOC Sensor, (b) transimpedance amplifier, (c) ADC expansion board, (d) Raspberry Pi, (e) Monitor Display

The downside of IoT Core is that it does not offer any data storage. Therefore, an event was created within IoT Core to send the data automatically to DynamoDB, whenever IoT receives a message. DynamoDB was chosen to store our data because it was a highly scalable, NoSQL database. NoSQL databases have fewer rules governing the data contained in the table than standard relational database models, allowing the ability to change what data was upload without having to keep up with multiple tables and complicated schemas. When the time comes to download the data, it behaves like relational databases, allowing SQL-like queries to filter through the data. The next step in the development process will be to use the AWS Python API to write a program to query data from DynamoDB, download it, and plot it automatically. This will allow easy remote monitoring of the sensor and allow multiple people secure access simultaneously. The first application of the IoT system was to read and store data from an AlGaN/GaN

triangular microcantilever VOC sensor. The only additional hardware needed for this application was a transimpedance amplifier to convert the output current from the VOC sensor into a voltage that the ADC could interpret. The measurement/processing/transmission (to Amazon cloud) setup and a typical sensing waveform output recorded back from Amazon cloud is shown in Fig 4.6.

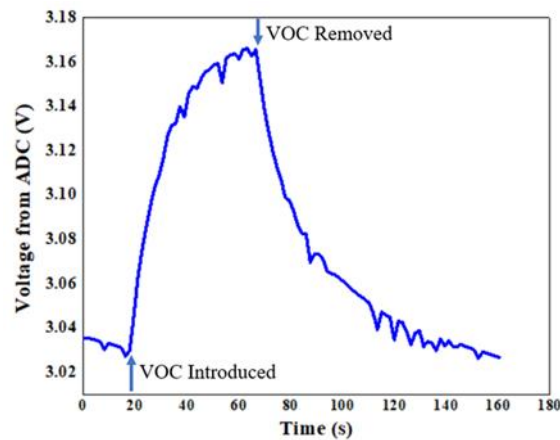


Figure 4.6: Data from DynamoDB showing sensor response to isopropanol

The Raspberry Pi also enables the data to be processed on the device itself, giving the option to alter sample sizes, compare multiple inputs, and filter out noise before sending it to the cloud. Eventually, computationally complex data processing will be needed from the microcontroller to identify compounds based on the characteristic sensor output associated with the different VOCs. Then the system will be ready to begin VOC monitoring at any WIFI accessible location. This is just one of many sensor applications that can be added to the Internet of Things via the Raspberry Pi and AWS platform.

CHAPTER FIVE

DUAL CHANNEL MICROCANTILEVER HEATERS

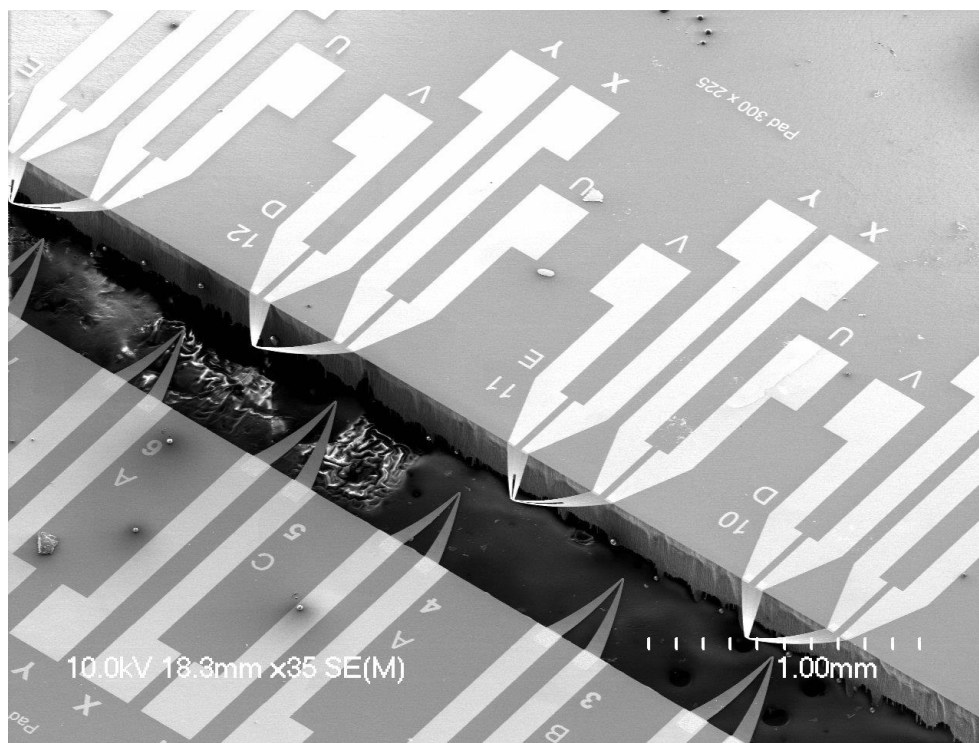


Figure 5.1: SEM Image of several dual channel microcantilevers

Monolithic tip dual channel microcantilever heaters (MDC-MHs; scanning electron micrographs shown in Fig. 5.1) not only offer a platform to perform VOC sensing utilizing separate functionalities of the two channels, but also present a unique geometry suitable for exploring the electrical breakdown characteristics of the GaN layer between the AlGaN/GaN channels.

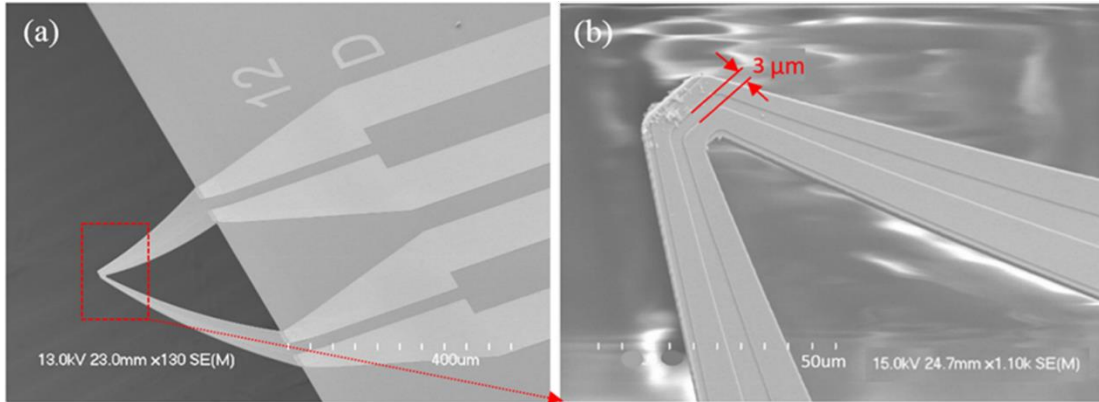


Figure 5.2: (a) SEM image of a monolithic tip dual channel microcantilever heater (MDC-MH), Ti/Au contacts, and substrate (b) SEM image showing the two parallel AlGaIn channels and the gap distance at the tip.

In this work, we have investigated the influence of polar VOC vapor exposure, in presence of an elevated temperature profile, on the critical breakdown voltage of inter-channel GaN layer in the MDC-MHs. A simple physical model has been proposed to explain the electrical breakdown of the inter-channel GaN layer, observed to be 50-fold lower than that of bulk GaN at room temperature. The inter-channel breakdown phenomenon, occurring at moderate bias voltages, presents a unique opportunity to devise a sensing scheme based on the inter-channel breakdown current (through GaN layer), which can increase by several orders of magnitude.

The MDC-MHs feature separate heating and sensing channels. The lower resistance inner channel served as the heating channel for the entire device, which enabled desired temperature to be reached at a lower bias voltage. The outer channel typically served as the sensing channel and is biased at 1 V to generate a high enough current to be monitored easily for VOC detection without causing any significant heating

effects [30]. The resistance curves of the inner and outer channel below the breakdown voltage are shown in Fig. 5.3

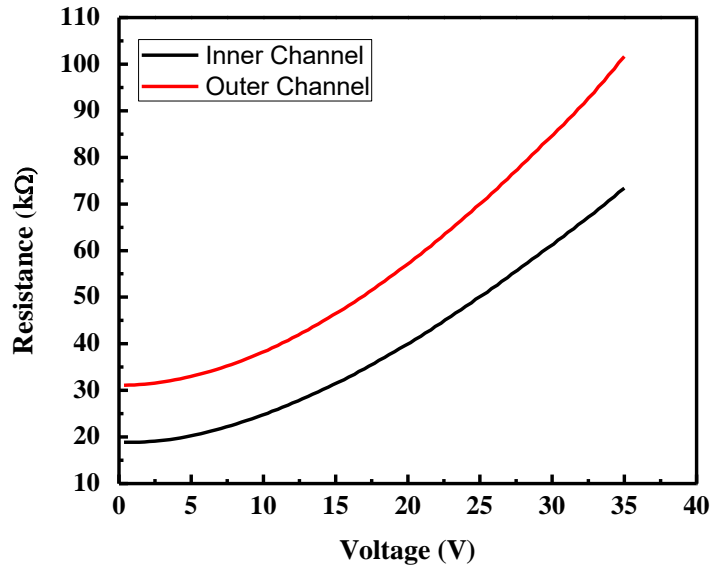


Figure 5.3: Resistance curves of the inner and outer channel below the breakdown voltage

Breakdown Characterization

Current-voltage (I-V) characteristics for the MDC-MHs were determined under dark, closed chamber conditions using both terminals of an Agilent B2900A Series Source/Measure Unit (SMU). The I-V characteristics recorded with the inner channel bias varied from 0 to 50 V are shown in Fig. 5.4(a). The outer channel was maintained at 1 V bias to monitor heating effects and record I-V characteristics. A schematic representation of the current flow directions in various channel sections of the MDC-MH before and after breakdown is shown in Fig. 5.4(b). Upon breakdown the two channels

become electrically connected at some location with the potential V_B [see Fig. 2(b)] allowing current to flow from the inner channel to the outer channel.

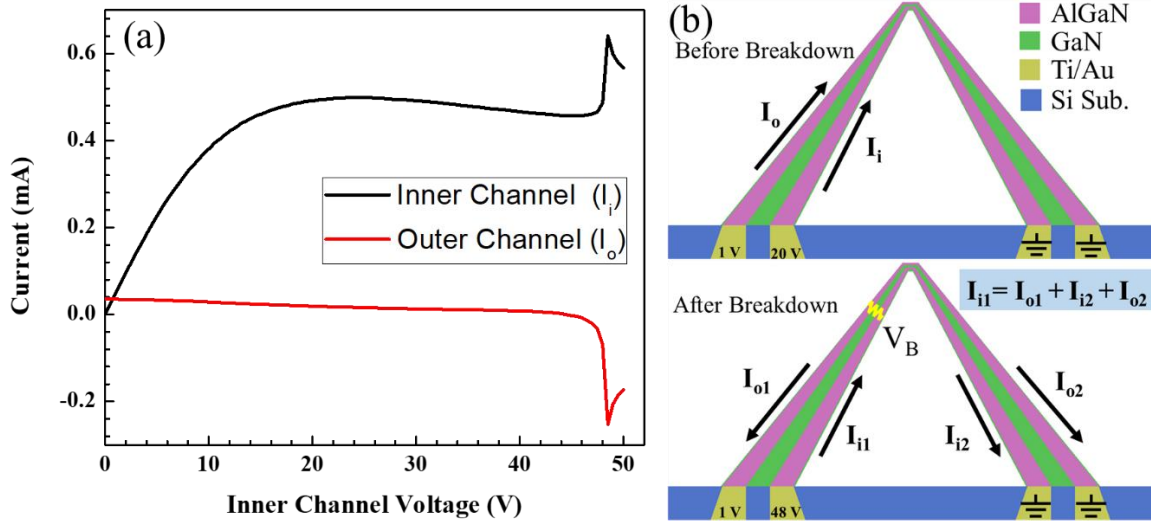


Figure 5.4: (a) Breakdown I-V characteristic of a monolithic tip dual channel microcantilever heater (MDC-MH) when 1 V is applied to the outer channel (b) Schematic of the currents in a MDC-MH at pre-breakdown and post-breakdown voltage biases.

The source current I_{i1} splits in three directions at the breakdown point with the relation $I_{i1} = I_{i2} + I_{o1} + I_{o2}$, where I_{i2} , I_{o1} , and I_{o2} are the different branch-off currents. Since the breakdown current I_{o1} in the left arm of the outer channel now opposes the current flowing there due to the outer channel bias of 1 V, the net outer channel current will be zero at some inner channel voltage. This inner channel voltage is defined as the “zero crossing” voltage (V_{ZC}) and has been used to differentiate the effect of VOCs (see discussion below).

For accurate estimation of the critical breakdown field (EB), as influenced by the geometrical and thermal effects, the outer channel terminals should be connected to

ground, shown in Fig. 5.5 inset. Before breakdown the measured outer channel current is typically in tens of nA, and we define the breakdown voltage as one where this pre-breakdown current increases by 100 times (reaching 1 μ A). The average inner channel breakdown voltage over the tested devices was ~ 39 V. Figure 5.5 shows a breakdown characteristic for a single device. Assuming the breakdown occurred where the GaN thickness is minimum at 3 μ m, and V_B is 39/2 or 19.5V, the EB for the inter-channel GaN layer is $(19.5\text{V}/3\mu\text{m}) = 6.5$ kV/cm, this is a factor of 50 less than bulk GaN, 3.3 MV/cm [22], [23]. It should be noted that due to high tip resistance and gradual change in the gap between channels near the tip, the breakdown voltage is likely higher than half the applied bias and breakdown field is underestimated to some extent.

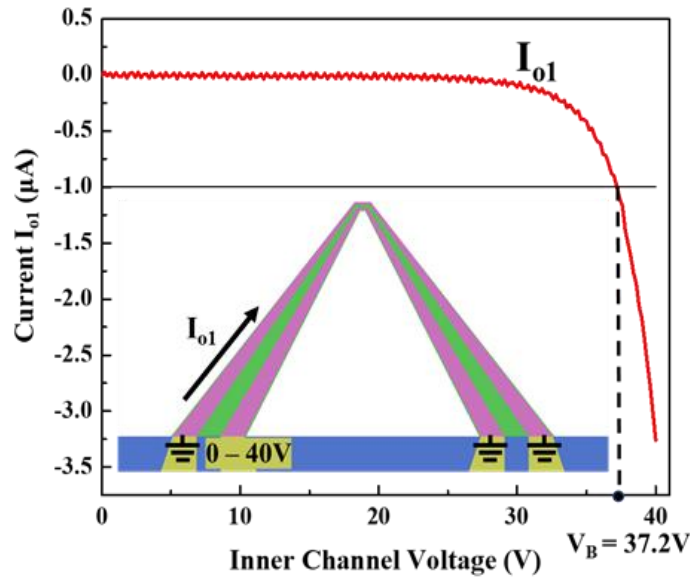


Figure 5.5: Breakdown current in the outer channel with 0V applied to the outer channel with line indicating the crossing of the 1 μ A threshold and the breakdown voltage indicated by V_B .

Although the EB of bulk GaN is reported as 3.3 MV/cm [22], [23], this number can change significantly for stressed thin films, as is the case for GaN cantilevers after removal from Si substrates [34]. Indeed, Wang showed for thin film GaN (2 μm) removed from the substrate the EB can be reduced by orders of magnitude, down to a few kV/cm. In addition, an elevated temperature profile can also reduce it significantly. Wang discovered that the breakdown voltage was reduced by more than 40% at 200 °C, as compared to 30 °C [35]. Elevated temperatures can cause multiple physical changes that may lead to early breakdown including hot electron effects, lowering of band gap, and defect/trap assisted tunneling [36] - [38]. In previous reports on the AlGaIn/GaN TMHs and MDC-MHs, the temperature of the tip was shown to exceed 300 °C [28], [29], which can contribute to significant lowering of EB.

VOC Sensing Results

To investigate the effect of VOCs on the breakdown characteristics of the MDC-MHs, three different VOCs (isopropanol, methanol, acetone) with characteristically distinct latent heats of evaporation were used in our studies. Saturated vapor (at 25°C) of each VOC was diluted with dry N₂ to a concentration of 25,000ppm using two different MFCs at appropriate flow settings [12]. The inner channel voltage of the device was swept from 0 to 40V during the vapor flow, while the outer channel voltage was maintained at 1V (see earlier discussion). Figure 5.6 shows the variation in outer channel current with inner channel voltage for all three VOCs (nominally at 25,000ppm) in comparison to the control characteristics, for a typical cantilever. At voltages below the breakdown voltage,

the control and VOC curves (in Fig. 5.6) are very similar, indicating that the reduction in current is due to heating and not due to the presence of VOCs.

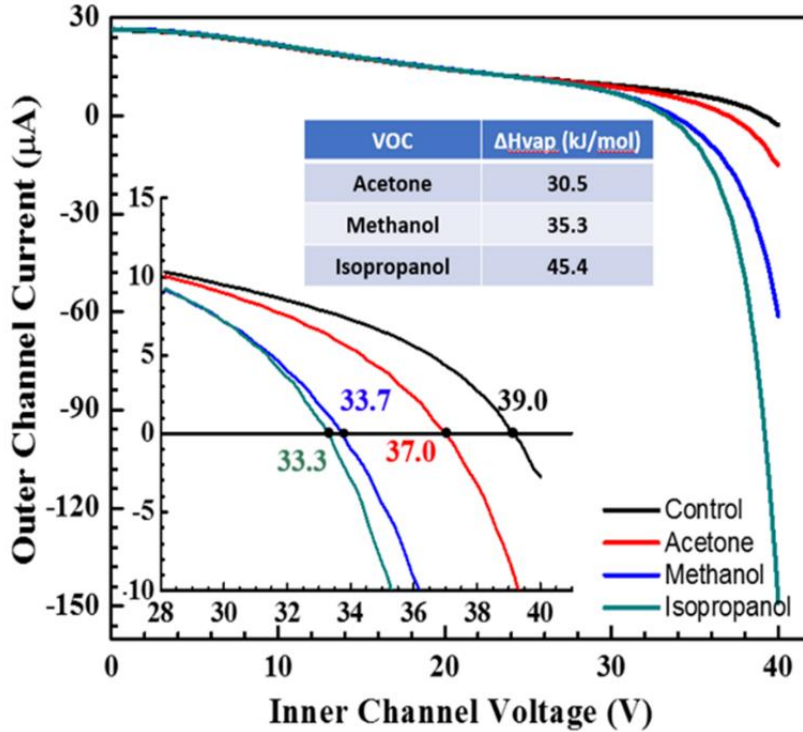


Figure 5.6: Current in the outer channel while in the inner channel is swept past breakdown in the presence of either neutral gas, acetone, methanol, or isopropanol. Inset: Close-up emphasizing the different zero-crossing point voltages of the different VOCs. Inset Table: Latent heat of evaporation (ΔH_{vap}) of relevant VOCs.

Once the swept voltage reaches $\sim 25V$ the VOC curves begin to differentiate from the control, but not enough from each other. Therefore, to have a proper definition to distinguish VOCs, we utilize the V_{ZC} (see earlier discussion). Isopropanol exhibits the lowest V_{ZC} of 33.3V, while acetone shows the highest V_{ZC} of 37V, with methanol in between at 33.7V (see Fig. 4 inset). As reported earlier, the latent heat of evaporation of a VOC can play a significant role in altering the thermal profile of a TMH [28]-[30], which can result in a change in the breakdown electric field of GaN. We have plotted the outer

channel currents, showing the V_{ZC} values for isopropanol for six different samples, which is shown in Fig. 5.7. We find that the V_{ZC} varies from 27.6 to 34.6 V for the set of samples tested, which can be attributed to potential variation in process parameters as well as AlGaIn thickness, as well as charge density and mobility variations due to non-uniformity in the CVD growth process. We would also like to note there that the microcantilevers used in this work went through several hundred cycles of testing with the VOCs, over a period of several months without any significant degradation in their characteristics.

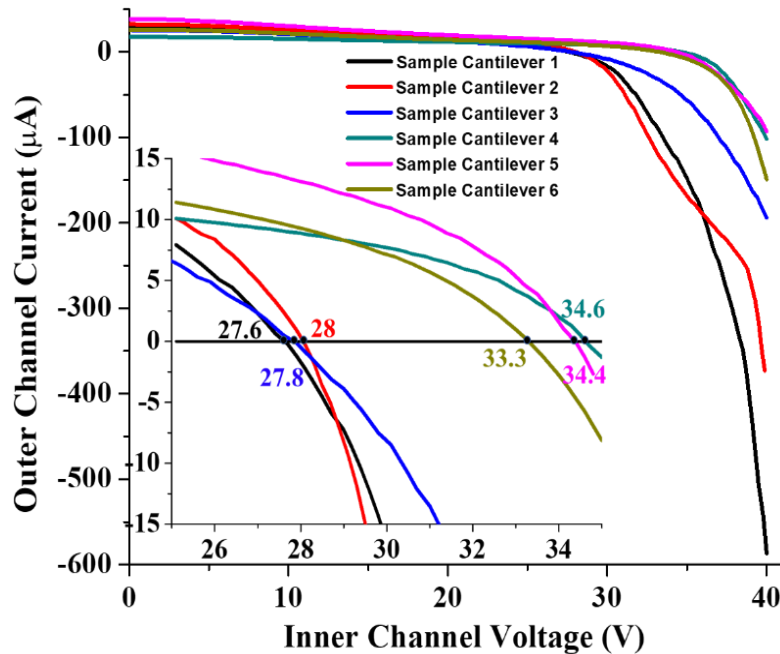


Figure 5.7: V_{ZC} values for 25,000 ppm isopropanol for six different sample cantilevers (SC)

We expect breakdown to happen on the high voltage side shifted from the apex, where a combination of high electric field and temperature makes it easiest for the GaN layer to break down. With the introduction of VOCs we expect the breakdown location to move

further away from the apex as the presence of VOCs has been shown to lower the apex temperature and increase the temperature in the adjacent region [28]. To check this hypothesis, we biased the inner channel at an appropriate voltage (slightly below the V_{ZC} of the control from Fig. 5.6), such that the introduction of a VOC would result in breakdown.

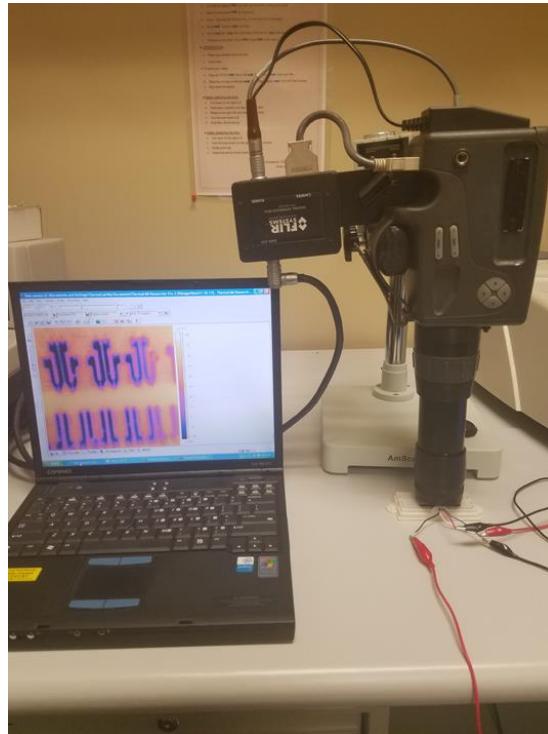


Figure 5.8: SC1000 Infrared microscope

To understand how breakdown voltage is affected by VOCs, the location of the breakdown on the cantilever was determined. Using a FLIR SC1000 infrared microscope (Fig. 5.8) we could observe the Joule heating profile of the TMH throughout the breakdown process. As expected, before the VOC was introduced, the highest temperature is recorded at the apex of the TMH and the distribution of heat is approximately symmetric, shown in Fig. 5.9b. Once the VOC is introduced a clear

difference in the temperature of the two sides of the cantilever about the tip is observed indicating that the point of breakdown is on the arm of the cantilever, not the tip region, Fig. 5.9c.

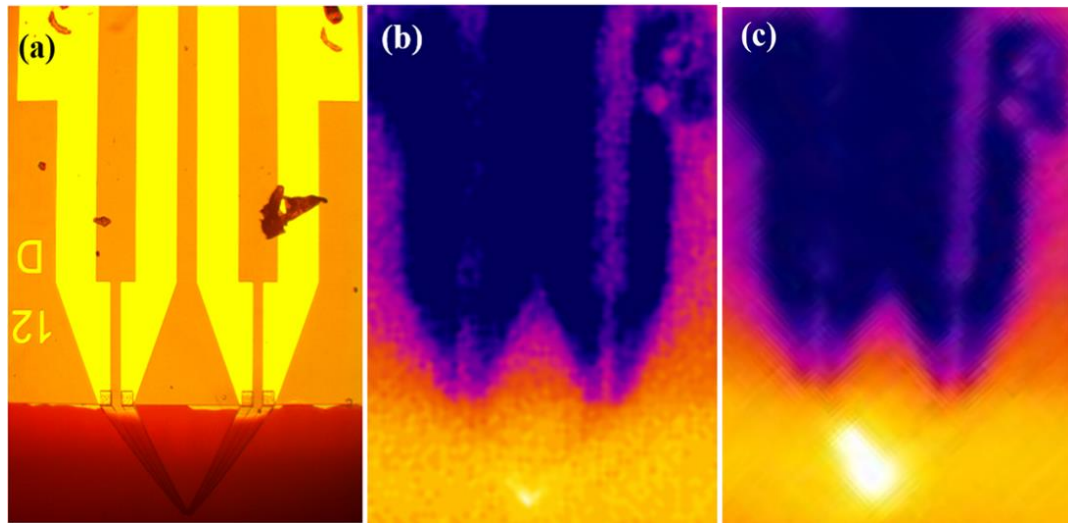


Figure 5.9: (a) Optical image of monolithic tip dual channel microcantilever heater (MDC-MH) (b) Infrared microscopy image of MDC-MH under pre-breakdown bias conditions (c) Infrared microscopy image of MDC-MH during breakdown.

As we move from the positive terminal of the inner channel to the tip of the cantilever the resistance along the path rapidly goes up. At the same time, the gap between the two channels decreases gradually, lowering the voltage required to cause avalanche breakdown. These two opposing trends make it possible to have a point along the cantilever arm where a lower resistance path can be formed for the inner channel current than continuing through the high resistance tip to ground. The current flowing into the outer channel via the breakdown point could go in two directions: towards the 1V terminal or the ground. Because of the location of the breakdown and since the path to

ground includes the high resistance tip region, most of the current will flow through the 1V terminal of the outer channel, resulting in the lopsided thermal profile.

Further investigation of the breakdown mechanism was done by measuring the current flow through all device terminals during a breakdown event. Isopropanol was chosen as the test VOC to initiate breakdown as it has the largest effect on shifting the breakdown voltage among the vapors tested (due to it having the largest latent heat of evaporation). With an inner channel biased at 38 V and outer channel at 1 V, the magnitude of the currents through all the terminals were recorded as the VOC (25,000 ppm isopropanol diluted in pure N₂) flow was started (~15 s) and stopped (~40s), as shown in Fig. 5.10. Prior to breakdown ($t < 18$ s) the input and output currents (I_{i1} and I_{i2} , respectively) at the inner channel are very close in magnitude, indicating that the inter-channel leakage current is very low, as expected. As breakdown occurs ($t > 20$ s) magnitude of I_{i1} and I_{i2} starts to differ very significantly, with the former increasing in magnitude and the latter reducing due to the introduction of the two outer channel paths to ground. It is interesting to note that the current through the 1 V terminal became approximately 5 times that of the grounded terminal (shown by I_{o1} and I_{o2} in Fig. 5.10). Therefore, breakdown must occur the left shoulder of the cantilever and not at the apex, which consequently attracted a lot more current to the 1V terminal compared to the 0 V terminal, as the 1V terminal offered a much lower resistance path for current flow. This clearly confirms our earlier postulation on the location of the breakdown point.

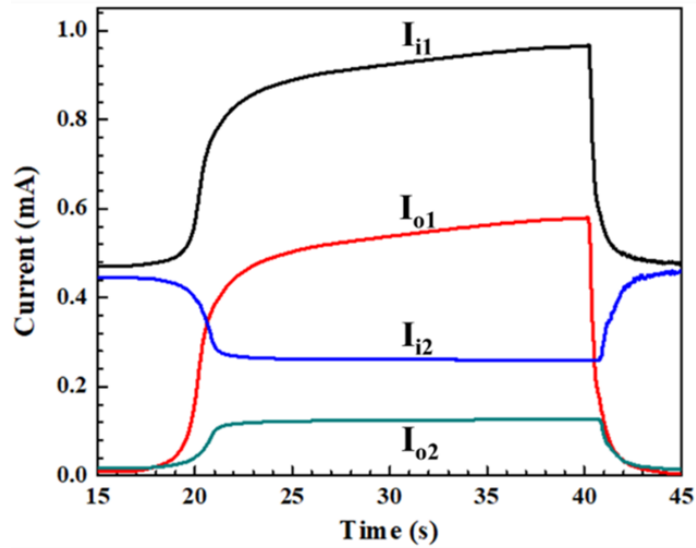


Figure 5.10: Current at all four terminals of a monolithic dual channel microcantilever heater (MDC-MH) when isopropanol is introduced at 15 sec. to induce breakdown until the system is purged with clean air at 40 s

The occurrence of inter-channel breakdown, with its consequent dramatic increase in breakdown current, offers interesting sensing possibilities. In previous sensing schemes using dual channel cantilevers, where breakdown did not occur, the sensor current merely changed by <5% in presence of VOCs [30]. This made it very challenging to detect low VOC concentration, especially in the sub-ppm range. In this work the current in the outer channel changes dramatically at breakdown offering the possibility to detect much lower concentration of VOCs. Figure 5.11 shows the variation in breakdown current ($I_{o1} + I_{o2}$) as the 25,000 ppm isopropanol is introduced into the sensing chamber, as well as when the VOC flow is replaced with purging N₂ flow. The pre-breakdown current ($I_{br,0} = I_{o1} + I_{o2}$) is $\sim 22 \mu\text{A}$, while the post-breakdown current increases dramatically to $\sim 650 \mu\text{A}$, which is a factor of 30 or 3000 % higher. Fig. 5.12 shows the amplification factor calculated as the ratio of the current at a given time with

the pre-breakdown current of 6.5 μA . Using the current change as the sensing parameter, much lower level of VOC may be detected (potentially in the low ppb level) than the 2000 ppm formerly demonstrated with $<5\%$ change in resistance [28].

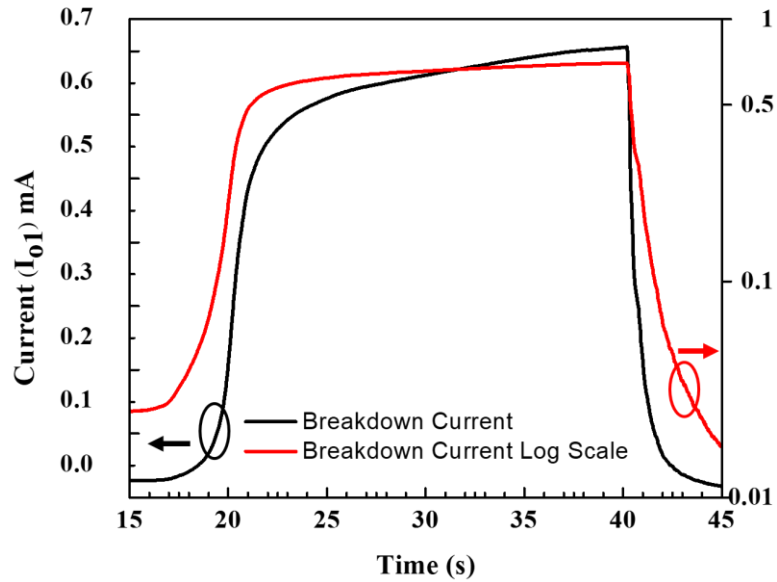


Figure 5.11: Breakdown current ($I_{o1} + I_{o2}$) in response to 25,000 ppm isopropanol

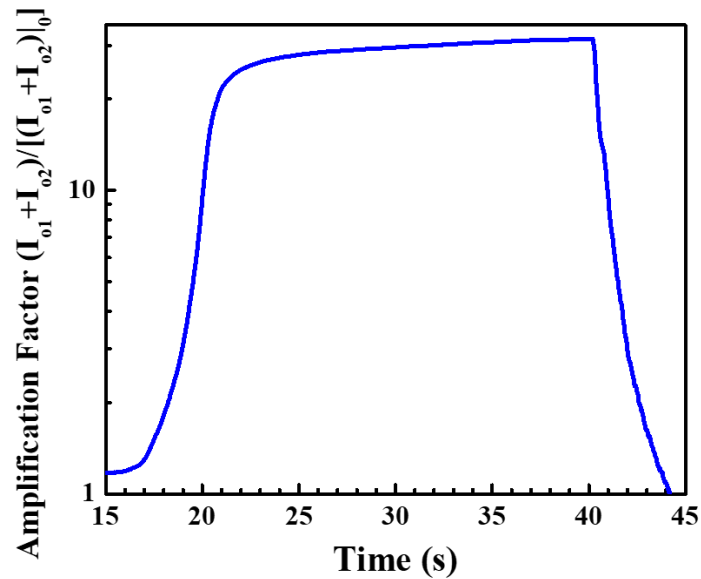


Figure 5.12: Amplification factor of the breakdown current ($I_{o1} + I_{o2}$) relative to the initial current pre-breakdown $(I_{o1} + I_{o2})_0$

This experiment was replicated using the analytes methanol and acetone, shown in Fig 5.13. However, due to their higher breakdown voltages compared to isopropanol, the 38V bias was less effective as causing immediate breakdown. Based on this information optimizing the bias voltage for breakdown is crucial for the effective sensing of all VOCs.

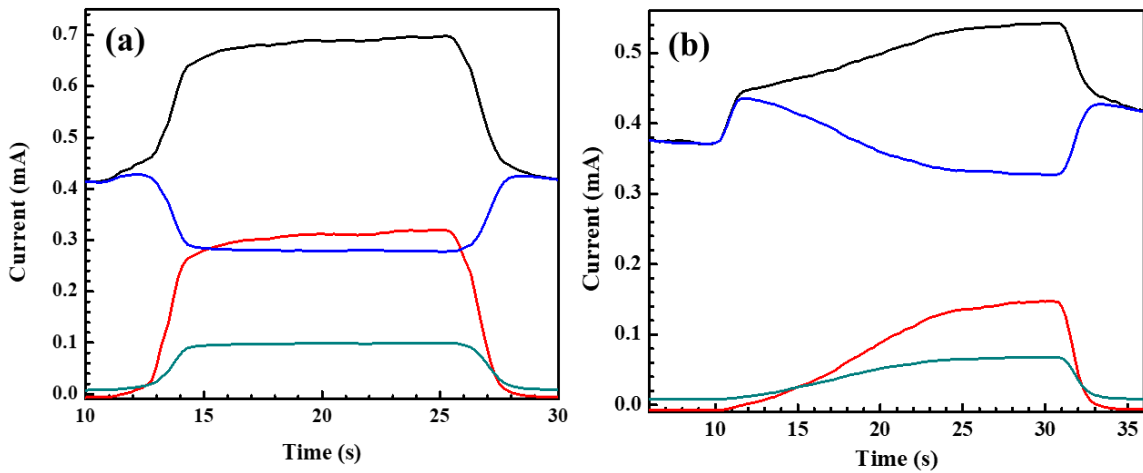


Figure 5.13: (a) Current at all four terminals of a monolithic dual channel microcantilever heater (MDC-MH) when methanol is introduced (b) acetone

In conclusion, we have investigated the reversible breakdown behavior of dual channel III-Nitride microcantilevers as influenced by the presence of multiple VOCs. The critical breakdown field of the inter channel GaN was found to be dramatically lower than bulk GaN due to dimensional and thermal effects, which got further lowered in the presence of VOCs, due to change in the thermal and electric profile near the cantilever apex. Different latent heats of evaporation of the VOCs resulted in varying magnitudes of breakdown voltage reduction, which can be used to preform selective detection of VOCs. Using the inter-channel current as a sensing parameter, which increased dramatically at

breakdown triggered by VOC exposure, can lead to their highly sensitive detection, to much lower levels than was previously demonstrated using these type of dual channel cantilevers.

CHAPTER SIX

MEASUREMENTS USING FIELD DEPLOYED COMMERCIAL SENSOR SYSTEM

Study of Environmental Parameters Triggering Asthma

In conjunction with the Greenville Health System a study was proposed to attempt to correlate medical incidents in children with a history of respiratory illness (such as asthma) to the air quality of their home environment on a weekly basis. Due to the immediate need and communication requirements a commercial air quality monitoring system was employed that was GPS and cellular network enabled. For this study the Airthinx™ system was employed because of its quality and wide range of sensors. The sensing capabilities include CO₂, CHO₂, VOC, particulate matter of 1 µm (PM1), PM2.5, PM10, temperature, humidity, and pressure.



Figure 6.1: Airthinx air quality monitoring system

Airthinx systems were employed at locations throughout the Greenville area as shown on the map in Fig 6.2. The systems were placed in the highest use area of the patients homes, typically the living room or kitchen.

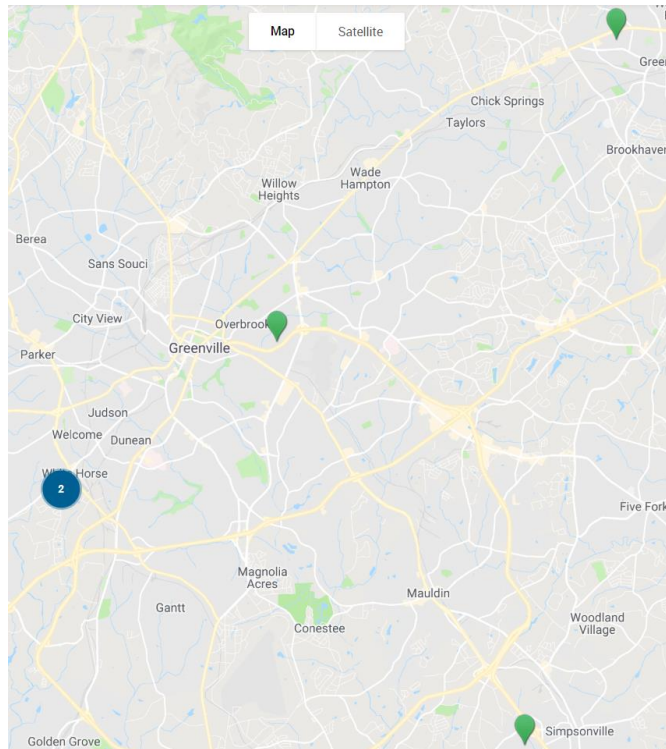


Figure 6.2: Map of deployed AirthinX systems

AirthinX Data Collection and Analysis

Onsite data was sent to the cloud via a cellular signal once a minute and updated to an online database provided by the company, examples of the weekly variation of formaldehyde (CHO_2) and PM_{10} are shown in Fig. 6.3 and 6.4.

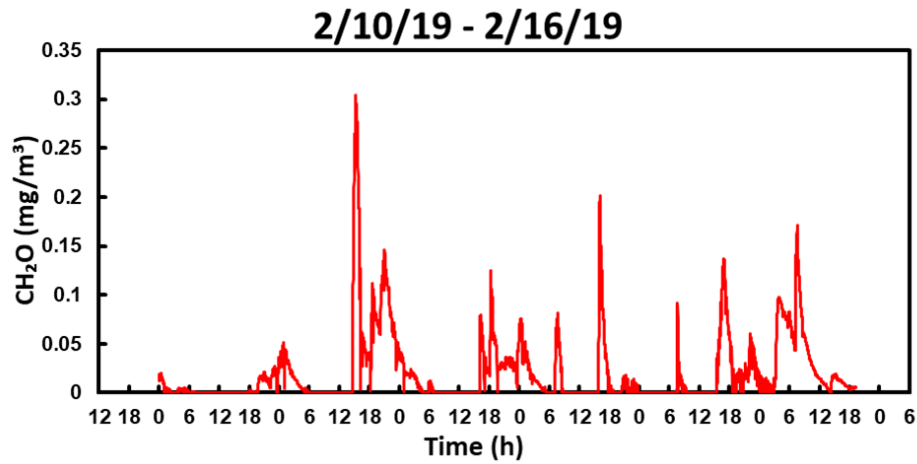


Figure 6.3: Example of the weekly variation of formaldehyde (CHO₂)

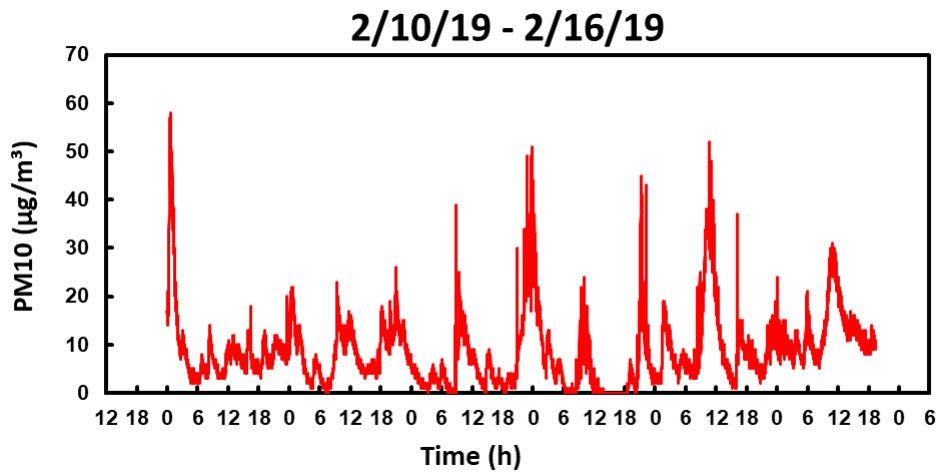


Figure 6.4: Example of the weekly variation of PM10

The VOC sensor employed by the Airthinx system is a chemiresistor that has been shown to be unreliable for the study. The CHO₂ sensor was more reliable and capable of detecting VOCs, so it replaced the VOC sensor for the study. Weekly averages of the different sensing parameters were compiled to be compared with patient medical scores from surveys that were also given weekly, the weekly averages of CHO₂ and PM10 for a patient are shown in Fig. 6.5 and 6.6.

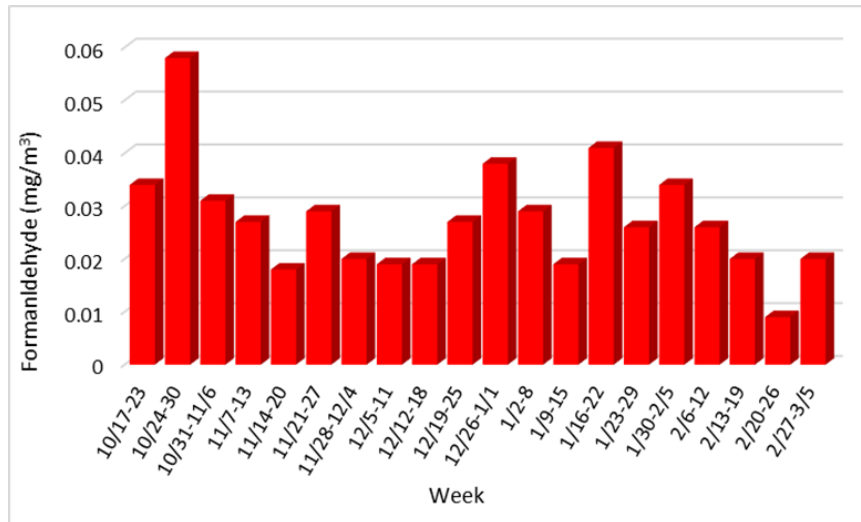


Figure 6.5: Weekly averages of formaldehyde (CHO₂) for a single patient

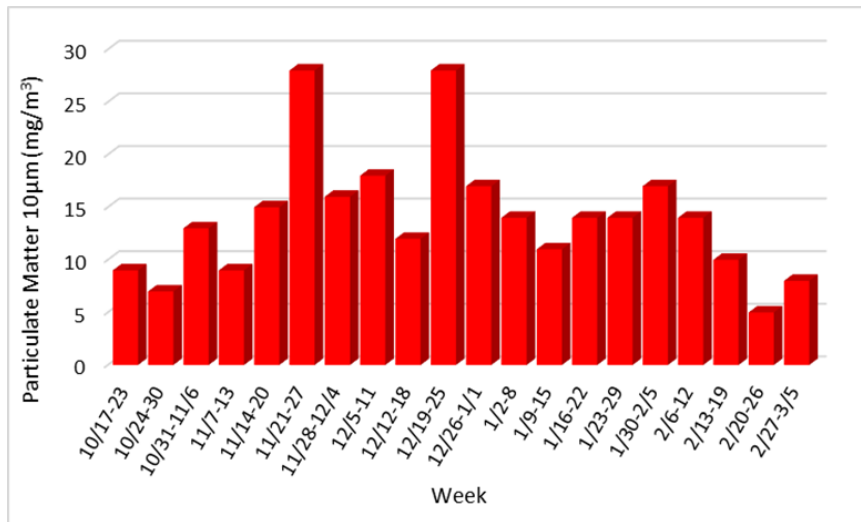


Figure 6.6: Weekly averages of PM10 for a single patient

The patients' parents were given a weekly survey to estimate, on a scale from 1-5, the severity of symptoms like cough, sputum production, wheeze, shortness of breath, and chest tightness. They were also asked if the patient used an inhaler and how many times, if the patient had to use oral steroids, and if the patient had to see a physician. A weekly total score based on the surveys will be determined after consulting with medical professionals and statistical analysis will be performed to look for any correlation

between the surveys and the Airthinx sensor system data. This study displays how VOC sensors can be used for the greater good and displays the shortcomings of current commercial VOC sensors.

CHAPTER SEVEN

CONCLUSIONS

Summary of Research

The ever-increasing problem of VOC exposure in humans needs to be addressed on many levels in our society. VOC sensors that are sensitive, selective, portable, and inexpensive could help bring about change by identifying sources of VOCs and displaying the ubiquity of these compounds in our indoor environments. In my research I have utilized the MEMs technology of microcantilever heaters and the AlGaIn/GaN materials system to sense VOCs. I have demonstrated how a single channel microcantilever can be used for identifying compounds based on the slope of current in response to VOC exposure. I then utilized the slope sensing to prototype a portable sensing system complete with air intake and display screen. With dual channel microcantilever heaters I demonstrated a novel GaN inter channel breakdown based VOC identification mechanism. The large sensing response to VOC with breakdown has implications for low concentration. Finally, I implemented a commercial sensor system for a real-world environmental monitoring application in an attempt to display the affects of VOCs the lives of patients.

Future Works

There are several directions that future work from this thesis can continue. The portable microcantilever heater based VOC sensing system can be updated to include the use of multiple sensors at once. Arduino code written for the system can be improved to directly calculate the slope of the VOC response or even the maximum slope of a VOC

response to predict what VOC is present. Testing with more VOC gases to make a library of the slope of the responses can be done to complete the system.

With the dual channel microcantilever heaters, an active biasing circuit to maintain the device on the edge of breakdown could be employed to maximize sensitivity. The resistance between the inner and outer channels could serve as the leg of a Wheatstone bridge and once breakdown occurs the massive change in resistance would give a large and easily measured voltage change at the output. The breakdown mechanism itself could have uses for other applications as well, such as working like a high voltage protection for other MEMs devices.

The study with the Greenville Health System will be continued and the sample size will continue to increase. To further increase the sample size and reduce the cost of doing so, a cheaper sensor system can be developed from commercial parts that only contains the sensors important to the study. Finally, a biostatistician could be employed to do a complete analysis of the data to look for trends in the sensors that could help predict and prevent medical incidents in high-risk patients.

APPENDICES

Appendix A

Code Used for Research

MATLAB CODE FOR CANTILEVER RESISTANCE MINIMIZATION

```
increment = 0.05; %Size step increment between
each test

RS = 460; %ohm/square %Sheet Resistance
TopW = 0.000003 * T; %Radius of tip of
cantilever
ITopW = 0.000001 * T;

for i = 1:1:40 %Variation Factor Range for
Total_Base
    for j = 1:1:20 %Variation Factor Range for
Total_Base
        for k = 1:1:50 %Variation Factor Range
for Total_Base

Total_Base = i*increment*330*10^(-6); %m %Full
width of cantilever touching the substrate
Height = j*increment*100*10^(-6); %m %Substrate
to inner side of tip
Channel_Base = k*increment*160*10^(-6); %m
%Width of single AlGaIn arm at the base

A2 = atan((Height-TopW)/((Total_Base/2) -
Channel_Base - ITopW)); %innermost angle of
cantilever
A3 = atan((Height-TopW)/((Total_Base/2) -
(Channel_Base/2) - (TopW/2) - ITopW)); %Bisects the
channel length

if A3 > 0 && A3 < 1.55
```

```

        ChannelLength = (Height-TopW)/(sin(A3));
%length of path electrons travel in 2DEG
        Lo = 0:0.1*10^(-6):ChannelLength;
        fun = @(Lo) 1./(Channel_Base-
2*(Lo.*cos(A3)-Lo.*sin(A3).*cot(A2)));
                if (Total_Base/2) -
(0.00002+Channel_Base) <= 0
                        LbyW = 0;
                else
                        LbyW =
integral(fun,0,ChannelLength);
                end
        R_arm(i,j,k) = RS * LbyW;
else
        R_arm(i,j,k) = 1;
end

if R_arm(i,j,k) >= 600 && R_arm(i,j,k) <= 1500
%Range of acceptable single arm resistance
        if Height >= 0.00009 && Total_Base <=
0.0005
                disp(Total_Base);
                disp(Height);
                disp(Channel_Base);
                disp(R_arm(i,j,k));
                end
        end
                end
                end
end

```

ARDUINO CODE FOR PORTABLE PROTOTYPE

```

#include <SPI.h>
#include <Adafruit_GFX.h>
#include <Adafruit_PCD8544.h>

```



```

#include <eRCaGuy_NewAnalogRead.h>

//Global variables
//Oversampling variables
  byte bitsOfResolution = 13; //commanded oversampled resolution
  unsigned long numSamplesToAvg = 16; //number of samples AT THE
OVERSAMPLED RESOLUTION that you want to take and average
  ADC_prescaler_t ADCSpeed = ADC_DEFAULT;

// Software SPI (slower updates, more flexible pin options):
// pin 7 - Serial clock out (SCLK)
// pin 6 - Serial data out (DIN)
// pin 5 - Data/Command select (D/C)
// pin 4 - LCD chip select (CS)
// pin 3 - LCD reset (RST)
Adafruit_PCD8544 display = Adafruit_PCD8544(7, 6, 5, 4, 3);

#define NUMFLAKES 10
#define XPOS 0
#define YPOS 1
#define DELTAY 2

#define LOGO16_GLCD_HEIGHT 16
#define LOGO16_GLCD_WIDTH 16

static const unsigned char PROGMEM logo16_glcd_bmp[] =
{ B00000000, B11000000,
  B00000001, B11000000,
  B00000001, B11000000,
  B00000011, B11100000,
  B11110011, B11100000,
  B11111110, B11111000,
  B01111110, B11111111,
  B00110011, B10011111,
  B00011111, B11111100,
  B00001101, B01110000,
  B00011011, B10100000,
  B00111111, B11100000,
  B00111111, B11110000,
  B01111100, B11110000,
  B01110000, B01110000,
  B00000000, B00110000 };

const int DELAY = 100;

```

```

const int ARRAYSIZE = 5;
float voltADC1[ARRAYSIZE];
float voltADC2[ARRAYSIZE];
float voltADC3[ARRAYSIZE];
float change1 = 0;
float change2 = 0;
float change3 = 0;
byte pin1 = A2;
int j;
int k;

void setup() {
  //Set up for oversampling
  //Configure the adc how you want it
  adc.setADCSpeed(ADCSpeed);
  adc.setBitsOfResolution(bitsOfResolution);
  adc.setNumSamplesToAvg(numSamplesToAvg);

  display.begin();
  // init done

  // you can change the contrast around to adapt the display
  // for the best viewing!
  display.setContrast(50);

  display.clearDisplay();

  display.setTextSize(1);
  display.setTextColor(BLACK);
  display.setCursor(0,0);

  for (j=0; j<5; j++) { //warmup ADC
    voltADC1[j] = adc.newAnalogRead(pin1);
    voltADC1[j] = 0;
    delay(DELAY);
  }

  analogReference(DEFAULT);
}

void loop() {
  for (j=0; j<(ARRAYSIZE); j++) { //create array of first values
    voltADC1[j] = adc.newAnalogRead(pin1);
    delay(DELAY);
  }
}

```

```

}

for (j=1; j<(ARRAYSIZE); j++) { //check if increasing
  if (voltADC1[ARRAYSIZE-j] > voltADC1[ARRAYSIZE-(j+1)]){
    k++;
  }
}

if (k >= (ARRAYSIZE-2)){
  for (j=0; j<(ARRAYSIZE); j++) { //create array of first values
    voltADC2[j] = adc.newAnalogRead(pin1);
    delay(DELAY);
  }

  k=0;
  for (j=1; j<(ARRAYSIZE); j++) { //check if increasing
    if (voltADC2[ARRAYSIZE-j] > voltADC2[ARRAYSIZE-(j+1)]){
      k++;
    }
  }
  if (k >= (ARRAYSIZE-2)){
    for (j=0; j<(ARRAYSIZE); j++) { //create array of first values
      voltADC3[j] = adc.newAnalogRead(pin1);
      delay(DELAY);
    }

    change1 = ((voltADC1[ARRAYSIZE-1]-voltADC1[0])/voltADC1[0])*100;
    change2 = ((voltADC2[ARRAYSIZE-1]-voltADC2[0])/voltADC2[0])*100;
    change3 = ((voltADC3[ARRAYSIZE-1]-voltADC3[0])/voltADC3[0])*100;

    display.println("VOC DETECTED");
    display.println(change1);
    display.println(change2);
    display.println(change3);
    display.display();

    delay(4000);

    display.clearDisplay();
    display.display();
    delay(1000);
  }
}
k = 0; }

```

REFERENCES

- [1] L. F. Liotta, "Catalytic oxidation of volatile organic compounds on supported noble metals," *Applied Catalysis B, Environmental*, vol. 100, (3), pp. 403-412, 2010.
- [2] R. Atkinson and J. Arey, "Atmospheric degradation of volatile organic compounds," *Chemical Reviews*, vol. 103, (12), pp. 4605-4638, 2003.
- [3] F. Davardoost and D. Kahforoushan, "Health risk assessment of VOC emissions in laboratory rooms via a modeling approach," *Environmental Science and Pollution Research*, vol. 25, (18), pp. 17890-17900, 2018.
- [4] Lerner, J.E.C., Kohajda, T., Aguilar, M.E., Massolo, L.A., Sánchez, E.Y., Porta, A.A., Opitz, P., Wichmann, G., Herbarth, O., Mueller, A. Improvement of health risk factors after reduction of VOC concentrations in industrial and urban areas. *Environ Sci Pollut Res* 21, 9676 (2014).
- [5] Guo, H., Lee, S, Chan, L. ., & Li, W. Risk assessment of exposure to volatile organic compounds in different indoor environments. *Environmental Research*, 94(1), 57 (2004).
- [6] Zhou, Y., Yu, J., Yan, Z., Zhang, C., Xie, Y., Ma, L., Li, F. Application of portable gas chromatography-photo ionization detector combined with headspace sampling for field analysis of benzene, toluene, ethylbenzene, and xylene in soils. *Environmental Monitoring and Assessment*, 185(4), 3037 (2013).
- [7] L. Spinelle et al, "Review of Portable and Low-Cost Sensors for the Ambient Air Monitoring of Benzene and Other Volatile Organic Compounds," *Sensors (Basel, Switzerland)*, vol. 17, (7), pp. 1520, 2017.

- [8] A. B. Kanu et al, "Ion mobility–mass spectrometry," *Journal of Mass Spectrometry*, vol. 43, (1), pp. 1-22, 2008.
- [9] Alifragis, Y., Georgakilas, A., Konstantinidis, G., Iliopoulos, E., Kostopoulos, A., & Chaniotakis, N. A. Response to anions of AlGa_N/Ga_N high-electron-mobility transistors. *Applied Physics Letters*, 87(25), 253507 (2005).
- [10] N. Kaur et al, "Branch-like NiO/ZnO heterostructures for VOC sensing," *Sensors & Actuators: B. Chemical*, vol. 262, pp. 477-485, 2018.
- [11] N. Shiraishi et al, "Fabrication and testing of polymer cantilevers for VOC sensors," *Sensors & Actuators: A. Physical*, vol. 202, pp. 233-239, 2013.
- [12] M. Z. Aslam et al, "FEM Analysis of Sezawa Mode SAW Sensor for VOC Based on CMOS Compatible AlN/SiO₂/Si Multilayer Structure," *Sensors (Basel, Switzerland)*, vol. 18, (6), pp. 1687, 2018.
- [13] M. Possas-Abreu et al, "Development of Diamond and Silicon MEMS Sensor Arrays with Integrated Readout for Vapor Detection," *Sensors (Basel, Switzerland)*, vol. 17, (6), pp. 1163, 2017.
- [14] S. Park et al, "CMUT-based resonant gas sensor array for VOC detection with low operating voltage," *Sensors & Actuators: B. Chemical*, vol. 273, pp. 1556-1563, 2018.
- [15] King, W. P., Kenny, T. W., Goodson, K. E., Cross, G. L. W., Despont, M., Durig, U. T., . . . Vettiger, P. (2002). Design of atomic force microscope cantilevers for combined thermomechanical writing and thermal reading in array operation. *Journal*

of Microelectromechanical Systems, 11(6), 765-774.

doi:10.1109/JMEMS.2002.803283

- [16] Lee, J., Beechem, T., Wright, T. L., Nelson, B. A., Graham, S., & King, W. P. (2006). Electrical, thermal, and mechanical characterization of silicon microcantilever heaters. *Journal of Microelectromechanical Systems*, 15(6), 1644-1655.
doi:10.1109/JMEMS.2006.886020
- [17] Dai, Z., Corbin, E. A., & King, W. P. (2010). A microcantilever heater–thermometer with a thermal isolation layer for making thermal nanotopography measurements. *Nanotechnology*, 21(5), 055503. doi:10.1088/0957-4484/21/5/055503
- [18] Lee, J., & King, W. P. (2008). Improved all-silicon microcantilever heaters with integrated piezoresistive sensing. *Journal of Microelectromechanical Systems*, 17(2), 432-445. doi:10.1109/JMEMS.2008.918423
- [19] Flack, T. J., Pushpakaran, B. N., & Bayne, S. B. GaN Technology for Power Electronic Applications: A Review. *Journal of Electronic Materials*, 45(6), 2673 (2016).
- [20] Simin, G., Jahan, F., Yang, J., Gaevski, M., Hu, X., Deng, J., Shur, M. III-nitride microwave control devices and ICs. *Semiconductor Science and Technology*, 28(7), 74008 (2013).
- [21] Stutzmann, M., Steinhoff, G., Eickhoff, M., Ambacher, O., Nebel, C. E., Schalwig, J., Müller, G. GaN-based heterostructures for sensor applications. *Diamond & Related Materials*, 11(3), 886 (2002).

- [22] Rais-Zadeh, M., Gokhale, V. J., Ansari, A., Faucher, M., Theron, D., Cordier, Y., & Buchaillet, L. Gallium Nitride as an Electromechanical Material. *Journal of Microelectromechanical Systems*, 23(6), 1252 (2014).
- [23] Dadgar, A. Sixteen years GaN on Si. *Physica Status Solidi (b)*, 252(5), 1063 (2015).
- [24] Offermans, P., & Vitushinsky, R. Detection with AlGaN/GaN 2DEG channels for air quality monitoring. *IEEE Sensors Journal*, 13(8), 2823 (2013).
- [25] Abdul Talukdar, M. Faheem Khan, Dongkyu Lee, Seonghwan Kim, Thomas Thundat and Goutam Koley, "Femtosecond displacement transduction using piezotransistive GaN microcantilever," *Nature Communications* 6, 7885 (2015).
- [26] Bayram, F., Khan, D., Li, H., Hossain, M. M., & Koley, G. Piezotransistive GaN microcantilevers based surface work function measurements. *Japanese Journal of Applied Physics*, 57(4), 40301 (2018).
- [27] Khan, D., Bayram, F., Gajula, D., Talukdar, A., Li, H., & Koley, G. Plasmonic amplification of photoacoustic waves detected using piezotransistive GaN microcantilevers. *Applied Physics Letters*, 111(6), (2017).
- [28] Jahangir, I., Quddus, E. B., & Koley, G. (2016). Unique detection of organic vapors below their auto-ignition temperature using III–V Nitride based triangular microcantilever heater. *Sensors and Actuators B: Chemical*, 222, 459 (2016).
- [29] Jahangir, I., & Koley, G. Modeling the performance limits of novel microcantilever heaters for volatile organic compound detection. *Journal of Micromechanics and Microengineering*, 27(1), 15024 (2016).

- [30] Jahangir, I., & Koley, G. (2016). Dual-channel microcantilever heaters for volatile organic compound detection and mixture analysis. *Scientific Reports*, 6(1). (2016).
- [31] Boeker, P. On “Electronic Nose” methodology. *Sensors and Actuators B: Chemical*, 204, 2 (2014).
- [32] H. Zhu et al, "Flow-through microfluidic photoionization detectors for rapid and highly sensitive vapor detection," *Lab on a Chip*, vol. 15, (14), pp. 3021-3029, 2015.
- [33] A. McWilliams, “U.S. Indoor Air Quality Market,” *Indoor Air Quality Solution Market Growth | BCC Research*. (2019).
- [34] Zimmermann, T., Neuburger, M., Benkart, P., Hernandez-Guillen, F.J., Pietzka, C., Kunze, M., Daumiller, I., Dadgar, A., Krost, A., & Kohn, E. Piezoelectric GaN sensor structures. *IEEE Electron Device Letters*, 27, 309 (2006).
- [35] Wang, T., Wang, B., Haque, A., Snure, M., Heller, E., & Glavin, N. Mechanical stress effects on electrical breakdown of freestanding GaN thin films. *Microelectronics Reliability*, 81, 181 (2018).
- [36] Hu, A., Yang, X., Cheng, J., Guo, L., Zhang, J., Feng, Y., Shen, B. Hot electron assisted vertical leakage/breakdown in AlGaIn/GaN heterostructures on Si substrates. *Superlattices and Microstructures*, 107, 240 (2017)
- [37] Nam, K. B., Li, J., Lin, J. Y., & Jiang, H. X. Optical properties of AlN and GaN in elevated temperatures. *Applied Physics Letters*, 85(16), 3489 (2004).
- [38] Chyi, J.-I., Lee, C.-M., Chuo, C.-C., Cao, X., Dang, G., Zhang, A., Wilson, R. Temperature dependence of GaN high breakdown voltage diode rectifiers. *Solid-State Electronics*, 44(4), 613 (2000).